

Dwarfs in nearby voids: results of SALT spectroscopy

S.A. Pustilnik,^{1*} A.Y. Kniazev,^{2,3,4} A.L. Tepliakova,¹ Y.A. Perepelitsyna,¹ E.S. Egorova^{4,5}

¹ *Special Astrophysical Observatory of RAS, Nizhnij Arkhyz, Karachai-Circassia 369167, Russia*

² *South African Astronomical Observatory, PO Box 9, 7935 Observatory, Cape Town, South Africa*

³ *Southern African Large Telescope Foundation, PO Box 9, 7935 Observatory, Cape Town, South Africa*

⁴ *Sternberg Astronomical Institute, Lomonosov Moscow State University, Universitetskij Pr. 13, Moscow 119992, Russia*

⁵ *Astronomisches Rechen-Institut, Zentrum für Astronomie der Universität Heidelberg, Mönchhofstraße 12-14, 69120 Heidelberg, Germany*

Accepted December ??, 2023, Received August 20, 2023

ABSTRACT

In the framework of the ongoing project, aimed at the systematical studying galaxies in nearby voids, we conducted spectroscopy with the Southern African Large Telescope (SALT) of 62 objects from the Nearby Void Galaxy (NVG) sample. They include 8 remaining objects of the 60 preselected candidates to eXtremely Metal-Poor (XMP) dwarfs, two known void XMP dwarfs and 52 void dwarfs residing within the Local Volume. For 47 galaxies residing in the nearby voids, we obtained spectra of the diverse quality. For 42 of them, we detected the Hydrogen and Oxygen lines that allowed us to get estimates of O/H in the observed HII regions. For 12 of the 42 objects, we detected the faint line [OIII] λ 4363, that allowed us to directly derive the electron temperature T_e and obtain their gas O/H by the direct method. 14 objects with the undetected [OIII] λ 4363 line fall to the lowest metallicities range ($12+\log(\text{O}/\text{H}) \lesssim 7.5$ dex). For them, we use a carefully checked new empirical ‘Strong line’ method of Izotov et al. For 14 other objects with only strong lines detected and with $12+\log(\text{O}/\text{H})$ of ~ 7.5 –8.0 dex, we used the modified version of ‘semi-empirical’ method of Izotov and Thuan. It accounts for effect of the excitation parameter O_{32} on T_e . 16 new galaxies are found with parameter $12+\log(\text{O}/\text{H}) \lesssim 7.39$ dex. Of them, four have $12+\log(\text{O}/\text{H}) = 7.07$ –7.20 dex. Of the 60 observed NVG objects, 15 have mistaken radial velocities in HyperLEDA. They do not reside in the nearby voids.

Key words: galaxies: dwarf – galaxies: evolution – galaxies: redshifts – galaxies: abundances – cosmology: large-scale structure of Universe

1 INTRODUCTION

Void represent the most rarefied and the largest volume elements of the Large-Scale Structure of the Universe. Despite galaxies residing in voids comprise a relatively small fraction of the whole realm of galaxies (van de Weygaert 2016), they are the important ‘bricks’ of our picture of the general galaxy evolution. Thus, Aragon-Calvo & Szalay (2013) predict the unusual properties of void structures and their galaxies due to the ‘time machine and cosmic microscope’ effects of the void environment.

A more detailed modelling of the void galaxy evolution is necessary to compare their predicted properties with the observed ones. In particular, one needs the high resolution simulations in order to address the small dwarfs with the baryonic mass of 10^6 – some $10^8 M_\odot$. Namely for this mass range, the observations (see below) demonstrate significant

differences with the properties of galaxies in denser environments.

The effect of environment on evolution is expected to be stronger for the lower mass objects. Since all known wide-area spectral sky surveys have the similar limiting apparent magnitude of B (or r) of ~ 18.5 , to have a representative galaxy sample to, e.g., $M_B = -10$ to -12 , one should explore the volume with the distances of $R \lesssim 20$ –25 Mpc. This choice differs substantially from many studies of void galaxy samples in more distant voids (~ 80 –200 Mpc), which probe properties of only the upper part of the galaxy luminosity function (e.g., Rojas et al. 2005; Patiri et al. 2006; Kreckel et al. 2012, and references therein).

An alternative approach related to the study of galaxies in the nearby voids, was suggested and partly realised by our group. The first step in this direction was the formation and studying of the galaxy sample in the nearby void Lynx-Cancer (Pustilnik & Tepliakova 2011; Pustilnik et al. 2016, and references therein). In particular, it was found that void galaxies as a whole are less evolved in average as compared

* E-mail: sap@sao.ru (SAP)

to the reference sample of the Local Volume (LV) late-type galaxies of Berg et al. (2012). They have elevated, in average, ratio of gas mass to luminosity ($M(\text{HI})/L_B$) (Pustilnik, Martin 2016) and the reduced gas metallicity (Pustilnik et al. 2016, 2021).

A surprising result of the above unbiased study of the whole Lynx-Cancer void sample was the discovery of several low-luminosity dwarfs with the eXtremely Metal-Poor (XMP) HII regions and the extremely-high gas mass fraction, $f_g = M_{\text{gas}}/M_{\text{baryon}}$, up to 0.97–0.99 (Pustilnik et al. 2010, 2011; Chengalur & Pustilnik 2013; Chengalur et al. 2017). Besides, an independently discovered XMP dwarf AGC198691 (Hirschauer et al. 2016; Aver et al. 2022) appeared to reside in the same void. We adopt here the definition of XMP galaxies as objects with $12+\log(\text{O}/\text{H}) \lesssim 7.21$ dex, or with $Z(\text{gas}) \lesssim Z_{\odot}/30^1$. This metallicity is close to that of the prototype of such unusual galaxies, the famous blue compact dwarf IZw18 (Searle & Sargent 1972).

In addition, these unusual dwarfs reveal blue colours of the outer parts of a galaxy (e.g. Perepelitsyna et al. 2014; Chengalur et al. 2017), where, in the framework of the common paradigm, the most aged stellar population resides. The colours, being compared to the evolutionary tracks from PEGASE2 package (Fioc & Volmerange 1999), correspond to the ages of the related stellar population of about one to several Gyr. That hints, along with the extremely high gas mass fraction, to the early stages of galaxy evolution.

These properties, in turn, may connect the unusual void dwarfs with the predicted so-called Very Young Galaxies (VYG) (Tweed et al. 2018), defined as objects, formed more than a half of stellar mass within the last 1 Gyr. While the other their properties are not specified in simulations, the first attempts to find such a rare population are presented by Mamon et al. (2020). Meanwhile, the comprehensive study of a void XMP dwarf IZw18 and its companion IZw18C gives a clear indication on their VYG nature (Papaderos & Östlin 2012).

The search for and the study of XMP dwarf galaxies was in focus of many groups since the discovery of the record low metallicity of IZw18. We already discussed recently the continuing efforts and findings of such unusual galaxies in the previous papers of this series. Therefore we refer a reader to these texts. The only remarks we would add to this issue, are the recent results of the search for new XMP dwarfs within the nearby voids (Pustilnik et al. 2020b, 2021). They appeared very promising, since the number of known such objects was doubled thanks to our conducted program during several last years.

However, one should note that the prominent XMP dwarfs in the local Universe are occasionally found also in a less rarefied environments. The known examples include 'Little Cub' galaxy (Hsyu et al. 2017) and 'Peekaboo' galaxy (Karachentsev et al. 2023) with $12+\log(\text{O}/\text{H}) = 7.11$ and 6.98 dex, respectively. This is not clear yet, whether their evolutionary paths differ from those for the similar objects in voids.

The voids themselves are not simple and homogeneous. They have the fine sub-structure resembling the Large-Scale

Table 1. Journal of SALT spectral observations. Main sample

No	Name	Date	Expos. time, s	PA	θ''	Air mass
1	J0015+0104	2019.10.01	2×1200	346.0	1.6	1.22
2	ESO294-010 ⁺	2020.12.18	2×1200	64.0	1.4	1.21
3	PGC004055 ⁺	2022.06.27	2×1200	66.0	1.7	1.27
4	UGC01085 ⁺	2022.11.22	2×1100	169.0	1.6	1.32
5	AGC124137*	2018.11.10	2×1200	238.0	1.6	1.34
	-#-	2019.09.02	2×1200	238.0	1.5	1.35
	-#-	2019.10.25	2×1200	238.0	1.7	1.34
6	ESO199-007 ⁺	2021.02.03	2×1200	13.0	1.5	1.33
7	PGC1166738* ⁺	2019.09.06	2×1150	41.5	1.6	1.22
	-#-	2019.12.25	2×1100	41.5	1.6	1.29
	-#-	2019.12.29	2×1100	41.5	1.7	1.29
8	PGC013294* ⁺	2019.09.01	2×1200	-24.0	1.1	1.27
9	PGC712531 ⁺	2021.07.31	2×1200	101.5	2.0	1.22
10	PGC681755 ⁺	2022.12.26	2×1300	51.0	1.2	1.27
11	ESO359-024 ⁺	2023.01.24	2×1200	255.5	1.7	1.28
12	PGC016389 ⁺	2023.02.22	2×1200	92.0	1.0	1.19
13	HIJ0517-32 ^{†+}	2022.01.06	2×1200	345.0	2.3	1.31
14	ESO553-046 ⁺	2023.01.25	2×1250	101.0	2.0	1.27
15	PGC138836 ⁺	2021.02.04	2×1150	161.0	2.0	1.31
	-#-	2021.02.07	2×1150	161.0	2.0	1.30
16	PGC018431 ⁺	2023.04.11	2×1200	87.0	1.8	1.23
17	ESO308-022 ⁺	2023.02.21	2×1200	331.0	1.9	1.28
18	PGC020125 ⁺	2022.12.18	2×1200	70.0	1.1	1.18
	-#-	2022.12.26	2×1200	70.0	1.2	1.21
19	J0935-1348	2013.12.28	3×800	0.0	1.7	1.25
20	PGC029033 ⁺	2023.01.21	2×1100	33.0	1.8	1.23
21	PGC041667 ⁺	2022.04.27	2×1100	293.5	1.5	1.27
22	PGC091215 ⁺	2022.03.05	2×1300	5.0	1.3	1.23
23	AGC227970 ⁺	2022.05.03	2×1200	40.0	1.9	1.30
24	AGC225197 ⁺	2022.03.05	2×1200	352.0	1.3	1.27
25	UGC07983 ⁺	2022.04.27	2×1100	5.0	1.1	1.33
26	PGC1289726 ⁺	2022.04.25	2×1100	38.0	1.3	1.27
27	AGC227972 ⁺	2022.04.26	2×1100	134.5	1.9	1.29
28	AGC227973 ⁺	2021.04.07	2×1100	326.0	1.4	1.28
	-#-	2021.06.13	2×1100	326.0	1.6	1.26
	-#-	2022.03.09	2×1100	326.0	1.3	1.28
29	AGC226122 ⁺	2023.01.31	2×1100	46.5	1.6	1.29
30	PGC1264260 ⁺	2021.02.06	2×1100	23.0	1.6	1.24
31	UGC08055 ⁺	2022.04.30	2×1100	97.0	1.3	1.33
32	PGC044681* ⁺	2023.02.23	2×1100	30.5	1.8	1.30
33	KKH86 ⁺	2022.05.31	2×1100	324.5	1.3	1.26
34	AGC716018*	2020.03.16	2×1150	41.0	1.6	1.30
35	AGC249197*	2019.05.29	2×1150	190.0	1.0	1.36
36	HIJ1738-57 ^{†*}	2019.05.03	2×1150	84.5	1.2	1.23
37	PGC408791 ⁺	2021.07.29	2×1150	279.5	1.4	1.27
	-#-	2021.11.06	2×1150	279.5	2.0	1.27
38	PGC129680 ⁺	2022.04.28	2×1100	45.5	1.0	1.29
39	PGC1016598*	2019.07.11	2×1300	103.0	1.8	1.30
40	ESO289-020 ⁺	2022.04.28	2×1100	331.5	1.4	1.23
41	ESO238-005* ⁺	2019.05.11	2×1100	47.0	1.6	1.22
42	PGC1028063 ⁺	2022.05.26	2×1100	300.0	1.2	1.20
43	ESO347-017 ⁺	2022.05.27	2×1100	90.0	1.2	1.21
44	PGC3192333 ⁺	2020.12.17	2×1100	265.5	1.4	1.22
45	PGC680341 ⁺	2020.12.15	2×1100	51.5	1.2	1.24
46	ESO348-009 ⁺	2022.05.31	2×1200	90.0	1.3	1.31
47	ESO149-003 ⁺	2022.06.06	2×1200	146.5	1.6	1.30

⁺ LV void galaxies; * XMP candidates from PEPK20;
[†] 'HIJ' means 'HIPASSJ'

¹ The solar value of $12+\log(\text{O}/\text{H})$ is adopted to be 8.69 dex after Asplund et al. (2009).

Structure of the Universe (e.g. Gottlöber et al. 2003; Aragon-Calvo & Szalay 2013). This sub-structure contains nodes, filaments and sub-voids. Therefore, one expects that properties of void galaxies can vary, in particular due to the different effects of their in-void *local* environments.

The first results, briefly summarised above, appeal to a much more massive studying of void dwarf galaxies. To address the diversity of void galaxies and to have an opportunity to compare cosmological simulations with the real void objects, one needs properties for a sample of many hundreds to thousands galaxies within the limited volume, unbiased as much as possible.

The natural questions related to such studies are the following: a) how much properties of void galaxies can differ from those in a more typical environment? b) how often properties of void galaxies *significantly* differ from those of a more common population? c) what empirical relations exist between the properties of void galaxies and other factors. The answers to these questions can help us to understand possible differences in formation and evolution scenarios of void galaxies from those in a more common environment.

As a development of the observational study of dwarf void galaxies, in order to increase substantially the statistics of such objects with known evolutionary parameters, $Z(\text{gas})$ and gas mass fraction, we formed a sample of 25 voids in the volume with $R < 25$ Mpc from the Local Group. We separate 1354 galaxies within this volume (~ 20 percent of the total number known in this volume) which fall within these nearby voids. We refer to this sample as the 'Nearby Void Galaxy' (NVG) sample (Pustilnik, Tepliakova & Makarov 2019, hereafter PTM19). The sample galaxies were collected mostly from the HyperLEDA data base (Makarov et al. 2014).

The main parameters of the parent NVG sample are as follows. The range of the absolute blue magnitudes is of $M_B = -7.5$ to -20.5 mag, with the median value of about -15.2 mag. The great majority of the NVG sample are the late-type galaxies (late spirals and dwarf irregulars), with the major fraction of the low surface brightness (LSB) galaxies. Similar to the wide range of luminosities, the distribution on the hydrogen mass in void galaxies is also very broad, with the full range of $M(\text{H I})$ of $10^{5.5} - 10^{9.7} M_\odot$, with the median $M(\text{H I}) \sim 10^{8.5} M_\odot$. The parameter of gas richness, the ratio $M(\text{H I})/L_B$ of about a thousand NVG sample galaxies with known HI data, spreads from 0.03 to 26, with the median of ~ 1 .

In the procedure of separation of void galaxies, all objects, appeared in the preselected empty spheres, were assigned to the void sample. They were further divided to the 'inner' void subsample ($\sim 80\%$), and the 'outer' subsample. The 'inner' 1088 galaxies reside in the 'inner' parts of voids. Their distances to the nearest luminous neighbours, delineating voids, $D_{\text{NN}} \geq 2.0$ Mpc, with the median value of ~ 3.4 Mpc.

The 'outer' 242 galaxies have $D_{\text{NN}} < 2.0$ Mpc, with the median of 1.65 Mpc. The separation of the void subsamples at $D_{\text{NN}} = 2.0$ Mpc was chosen to be consistent with the definition of galaxies residing in the nearby Lynx-Cancer void from our previous study (Pustilnik & Tepliakova 2011; Pustilnik et al. 2016). In that work, the border of $D_{\text{NN}} > 2.0$ Mpc was tentatively chosen so that to study the well defined void objects and to exclude possible interlopers. The study of both, the 'inner' and the 'outer' subsamples, will al-

low one to understand how many of the 'outer' void galaxies represent on their properties an 'intermediate' kind of the galaxy population in the context of transition between the lowest density regions and the walls, with a roughly mean matter density.

We then began two projects based on this sample. One of them is the search for new XMP void dwarfs. We selected 60 candidate XMP dwarfs from the whole NVG sample based on their known properties in the open data bases and in the literature (Pustilnik et al. 2020a). The results of spectroscopy of $\sim 3/4$ of them are presented in papers Pustilnik et al. (2020b, 2021).

Another project is devoted to the study of the subsample of the NVG objects which fall within the LV. This consists of ~ 260 objects from the NVG at the distances closer than 11 Mpc. First results on this part were presented in Pustilnik et al. (2022a,b). This is an analogue of our unbiased study of the galaxy sample in the nearby void Lynx-Cancer. The northern part of void galaxies in this project is studied at the SAO 6-m telescope BTA. The detailed description of the LV void sample, with some intermediate results, will appear in a paper in preparation.

Here we present the results of the Southern African Large Telescope (SALT; Buckley, Swart & Meiring 2006; O'Donoghue et al. 2006) spectroscopy from the both projects. The first part includes eight of the remaining 14 dwarfs selected in Pustilnik et al. (2020a) as the void XMP candidates. The second part includes 49 galaxies selected as residing in voids within the LV, mainly the least luminous dwarfs. Also, a known XMP dwarf J0015+0104 from the Eridanus void (Guseva et al. 2009; Pustilnik et al. 2013) was observed to improve the accuracy of its O/H.

The content of the paper is arranged as follows: the description of the SALT spectral observations and data processing is presented in Sec. 2. In Sec. 3 we give the description of emission line measurements and methods used for O/H determination. The estimates of O/H for the observed galaxies are shown in Sec. 4. In Sec. 5 we discuss the obtained results along with other available information. In Sec. 6 we summarise and conclude. In the on-line supplementary materials we present the following data. In Appendix A we provide finding charts of all observed galaxies with the spectrograph long slit position superimposed. In Appendix B, plots of 1D spectra for the observed galaxies are presented. Appendix C presents the tables with line intensities, derived physical parameters and the values of $12+\log(\text{O/H})$.

2 SALT OBSERVATIONS AND DATA PROCESSING

For our spectral observations we used the Southern African Large Telescope (SALT; Buckley, Swart & Meiring 2006; O'Donoghue et al. 2006) in service mode in the period from May 2019 to April 2023. Several of the 64 target galaxies were observed from two to three times in order to increase the S-to-N ratio of the 'strong' lines in the potentially very low-metallicity objects. The obtained spectra were averaged for the subsequent analysis. See Tables 1, 2. The SALT Robert Stobie Spectrograph (RSS; Burgh et al. 2003; Kobulnicky et al. 2003) was used with VPH grating PG0900 with the long slit of $1.5''$ by $8'$. This option provides the

range from 3600 Å to 6700 Å and the spectral resolution of FWHM~6.0 Å. For the obtained 2D spectra, we used a binning factor of four for the spatial scale and factor of two for the spectral coordinate. This gives us a final spatial sampling of 0''.51 pixel⁻¹ and spectral sampling of 0.97 Å pixel⁻¹.

Spectral observations with the sufficiently small entrance hole or with the narrow slit are the subject of the differential atmospheric refraction (e.g., Filippenko 1982). To minimise its effect on the wavelength-dependent light loss, the long slit position angle (PA) is recommended to keep close to the direction of the atmospheric refraction (parallactic angle). In many cases, this can substantially limit the efficiency of observations. The RSS is equipped with an Atmospheric Dispersion Compensator (ADC), what allowed us not to worry about the effect of atmospheric refraction at arbitrary long-slit PAs. Spectrophotometric standards were observed during every night as a part of the SALT standard calibrations program.

In order not to repeat literally the description of specifics of SALT observations and flux calibration, we refer a reader to Section 2 of our recent paper (Pustilnik et al. 2020b).

The majority of HII-regions in the observed galaxies are faint and low-contrast. For the pointing, we used nearby offset stars. In most cases, we selected position angles (PAs, in degrees) of the slit so that to include a nearby offset star and to cover a faint HII-knot in a program galaxy. See the journals of observation in Tables 1, 2. They present the main information on each observation: the dates of observations, exposure times, seeing θ (in arc seconds) and air mass.

Since many of the observed dwarfs are faint and of low surface brightness, an attempt to obtain their independent spectra can be a problem. To ease independent checks of our data, we present in Tables 1, 2 the used long slit position angles (PA). In Figures A1 – A4 of the on-line materials, we show their images with superimposed long slit positions. All but a few images are taken from the Legacy surveys database (Dey et al. 2019) The remaining several images which are unavailable in the Legacy database, are taken from the ESO Online archive (<https://archive.eso.org/dss/dss>).

Similar to our previous paper (Pustilnik et al. 2020b), the SALT science pipelines (Crawford et al. 2010) were used for the primary data reduction. For each CCD amplifier, they include bias and overscan subtraction, gain and cross-talk corrections and finally, mosaicing. The following long-slit reduction was conducted as described in the paper by Kniazev (2022).

3 LINE MEASUREMENTS AND O/H DETERMINATION

The emission line fluxes obtained from 1D spectra were measured as described in detail in Kniazev et al. (2004) and briefly summarised in Pustilnik et al. (2020b). In order not to repeat this description, we refer a reader to these papers. Very briefly, the procedures include the robust drawing of

Table 2. Journal of SALT spectral observations. Objects with wrong velocities

No.	Name	Date	Expos. time, s	PA	θ''	Air mass
1	PGC3197756 ⁺	2021.09.10	2×1200	295.0	1.8	1.27
2	PGC901638 ⁺	2021.08.03	2×1200	314.5	1.3	1.23
3	PGC3207684 ⁺	2021.10.08	2×1150	259.0	1.3	1.22
4	PGC3210819 ⁺	2021.08.04	2×1200	317.0	1.8	1.22
5	PGC504827 ⁺	2021.08.01	2×1200	282.5	1.3	1.25
6	PGC645417 ⁺	2022.01.23	2×1150	48.0	2.2	1.28
7	PGC016383	2023.02.22	2×1200	92.0	1.0	1.19
8	AGC208329 ⁺	2019.01.06	2×1200	94.5	1.5	1.29
9	J1355+04B†	2022.05.31	2×1100	73.0	1.0	1.31
10	PGC1069207 ⁺	2021.04.14	2×1100	137.0	1.2	1.21
11	PGC264615 ⁺	2021.04.04	2×1200	21.0	1.3	1.32
	-#-	2022.04.12	2×1200	21.0	1.5	1.35
12	PGC064718 ⁺	2023.04.02	2×1200	52.0	1.4	1.31
13	PGC162688 ⁺	2021.08.02	2×1200	107.0	1.6	1.26
14	PGC163318 ⁺	2021.07.17	2×1200	43.0	2.0	1.23
15	6dFJ2226-2916 ⁺	2020.11.13	2×1200	23.0	1.8	1.21
16	ABELL3888.14 ⁺	2021.07.30	2×1200	337.5	1.3	1.24
17	ABELL3888.12 ⁺	2021.08.03	2×1200	134.0	1.5	1.23

⁺ selected as the LV void galaxies

† Makarov & Uklein (2012) adopt it as a companion of KKH86

continuum with the subsequent use of MIDAS²-based programs for determination of parameters of emission lines.

Giving the line fluxes measured, we utilise an iterative procedure from Izotov et al. (1994), which accounts for the total sight-line dust extinction and the underlying Balmer line absorptions originating in the related young stellar clusters. As a result, it provides the simultaneous estimate of the equivalent width of absorption Balmer lines $EW(abs)$ and the extinction coefficient $C(H\beta)$. The relevant equation (1) from Izotov et al. (1994) was used:

$$I(\lambda)/I(H\beta) = [EW_e(\lambda) + EW_a(\lambda)]/EW_e(\lambda) \times \\ EW_e(H\beta)/[EW_e(H\beta) + EW_a(H\beta)] \times \\ F(\lambda)/F(H\beta) \exp[C(H\beta)f(\lambda)] \quad (1)$$

Here $I(\lambda)$ is the intrinsic line flux corrected for the over-all extinction (both in the Milky Way and internal to a particular galaxy or HII region) and the underlying Balmer absorption, while $F(\lambda)$ is the measured line flux. Here, as in Izotov et al. (1994), $EW_e(\lambda)$ are equivalent widths of used emission lines. $EW_a(\lambda)$ is the adopted value of the underlying Balmer absorptions. The theoretical Balmer line ratios $I(\lambda)/I(H\beta)$ for Case B from Brocklehurst (1971) were used for iterative procedure with equation (1).

Following to Izotov et al. (1994), this term is used to estimate intrinsic fluxes only for Balmer emission lines. Similar to this paper, we adopt the reddening function $f(\lambda)$ from Whitford (1958). It is normalised so that $f(H\beta) = 0$. For

² MIDAS is an acronym for the European Southern Observatory package – Munich Image Data Analysis System.

this $f(\lambda)$, there is a relation between the excess $E(B - V)$ and $C(H\beta)$: $E(B - V) = 0.68 \times C(H\beta)$.

In the classic (T_e) method of the oxygen abundance determination, they use the standard two-zone model and method of Aller (1984). Since the electron temperature T_e is different in high and low-ionisation HII regions (e.g. Stasińska 1990), to calculate abundances of ions O^{++} and O^+ , one needs to know temperature T_e in both parts of an HII region. The estimate of $T_e(O^{++})$ uses the flux ratio of [OIII] lines: $I(\lambda 4363)/I([\lambda 4959 + \lambda 5007])$ and the five-level atom model (Aller 1984), with the electron density N_e derived from the line ratio of the [SII] doublet: $I(\lambda 6717)/I(\lambda 6731)$. Since in our spectra this doublet was outside the range, we adopted for further calculations $N_e = 10 \text{ cm}^{-3}$, a typical electron density in HII regions of dIrr galaxies. To derive $T_e(O^+)$, we used the fit for the relation between $T_e(O^+)$ and $T_e(O^{++})$ from Izotov et al. (1994), based on the models of photoionised HII regions by Stasińska (1990). This fit is read as follows:

$$t_e(\text{OII}) = 0.243 + t_e(\text{OIII})[1.031 - 0.184 t_e(\text{OIII})] \quad (2)$$

Here $t_e = 10^{-4} T_e$. The resulting rms uncertainty of $t_e(\text{OII})$ is transferred from the corresponding rms error of $t_e(\text{OIII})$ as derived with use of the above relation. The ionic abundances of O^+/H^+ and O^{++}/H^+ are calculated with formulae (3) and (5) from Izotov et al. (2006).

The major part of HII regions in the studied galaxies are rather faint. Accordingly, the fluxes of their emission lines are low. The weak auroral line, [OIII] $\lambda 4363 \text{ \AA}$, which is used in the 'direct' (T_e) method for the determination of the electron temperature T_e , was detected only in the minority of our targets. Therefore, for the estimate of O/H in the remaining galaxies, we applied the semi-empirical method of Izotov & Thuan (2007). However, as was shown in Pustilnik et al. (2021), this method provides the reliable estimates of T_e in rather limited range of parameters of HII regions. We modified their method, as described in Pustilnik et al. (2021), in order to expand its applicability to the wider range of physical conditions.

The basement of method of Izotov & Thuan (2007) is the fitted empirical dependence between the values of the electron temperature T_e and parameter R_{23} . It was derived from the analysis of the grid of models of HII-regions in Stasińska & Izotov (2003). As the authors find, for the large representative sample of extragalactic HII-regions, which cover the whole range of observed O/H, the models approximate well the apparent relations of the strong line intensities versus $EW(H\beta)$. The parameter R_{23} is the ratio of the sum of fluxes of strong oxygen lines [OII] $\lambda 3727 \text{ \AA}$, [OIII] $\lambda 4959 \text{ \AA}$, [OIII] $\lambda 5007 \text{ \AA}$ to that of $H\beta$. When T_e is estimated via R_{23} , the rest of the calculations of the ionic abundances of O^+/H^+ and O^{++}/H^+ uses the standard equations of the classic T_e method, that is the same formulae (3) and (5) from Izotov et al. (2006).

As it became clear later, the good approximation of O/H, derived by this method, to O/H values, obtained by the direct method, has the limited application. This is because it was fitted from a sample of HII-regions with a rather limited range of the excitation parameter O_{32} (the ratio of line fluxes of [OIII] $\lambda 5007$ and [OII] $\lambda 3727$). This parameter is a proxy of the physical parameter U - so-called the ionisation parameter, characterising the flux of ionising photons per unit area of the illuminated gas cloud surrounding the

central source. While the original method of Izotov & Thuan (2007) works well for the intermediate values of O_{32} ($\sim 2-6$), it leads to the significant systematical bias in the T_e and O/H estimates at both, small and large values of O_{32} . The whole range of O_{32} in known HII regions spreads from $\lesssim 0.3$ to ~ 50 .

This effect was examined in Pustilnik et al. (2021) on the large sample of HII-regions with O/H derived via the direct method. The sample covers the broad range of parameter O_{32} and O/H. The modified formula was suggested to estimate T_e , which includes the dependence of T_e on the both parameters, R_{23} and O_{32} . The respective method is called the modified semi-empirical (mse). The mse method has the moderate internal scatter in $\log(O/H)$ of 0.09 dex, while allows one to eliminate the systematic bias of the original method of Izotov & Thuan (2007) for the extreme values of parameter O_{32} .

This is crucial for our project, since the typical HII-regions in our void galaxy sample, in which the auroral line [OIII] $\lambda 4363$ was too noisy or undetected, have rather low excitation parameter, of $O_{32} \lesssim 1.0$. The O/H estimates derived by this method are marked as (mse) in Column 9 of Table 3.

Recently Izotov et al. (2019) suggested a new empirical method, the best suited for HII-regions with 'metallicity' $12+\log(O/H) \lesssim 7.4$ dex. This uses only the relative fluxes of strong Oxygen lines with respect of $H\beta$. Namely, their Equation (1) reads as:

$$12 + \log(O/H) = 0.950 \times \log(R_{23} - 0.08 \times O_{32}) + 6.805$$

This relation, calibrated on the large number of HII-regions with O/H derived via the direct (T_e) method, empirically accounts for the large scatter in the ionisation parameter $\log(U)$ (from about -4 to -1) in various HII-regions and, thus, reduces the relatively large internal rms scatter of the other empirical methods based on the strong oxygen lines, down to only ~ 0.04 dex. The latter value of the rms scatter was obtained in Pustilnik et al. (2021) on the sample of ~ 70 HII-regions with the range of $7.0 \lesssim 12+\log(O/H) \lesssim 7.5$ dex. However, its applicability is limited only to the range of $12+\log(O/H) \lesssim 7.5$. The above relation was slightly modified by Izotov et al. (2021) to account HII regions with the highest observed values of O_{32} .

Among our galaxies there are 16 objects falling to this category. For them, we use this method. For derived this way value of O/H, we attach index (s) in Column 9 of Table 3, and denote them hereafter as O/H(s).

As shown in Pustilnik et al. (2021), there is a tiny offset in the zero-point of $12+\log(O/H)(s)$ relative to that of $12+\log(O/H)(T_e)$, of ~ 0.01 dex. In Table 3, we present therefore the values of $12+\log(O/H)(s)$ with the subtraction of 0.01 dex from the values obtained with the formula from Izotov et al. (2019). This allows us to compare them directly with the estimates of $12+\log(O/H)(T_e)$ for other galaxies.

The contribution of errors in the strong line fluxes to the related uncertainty of $12+\log(O/H)(s)$, $\sigma_{\log(O/H)}$, is rather modest. For the high S-to-N spectra with $\sigma_{R_{23}}/R_{23} < 0.02$, the total $\sigma_{\log(O/H)}$ is close to the internal error of the method, namely, $\sigma_{\log(O/H)} \sim 0.04$ dex. For the lowest S-to-N our spectra of $\sigma_{R_{23}}/R_{23} \sim 0.14$, the error of $\log(O/H)(s)$ increases to 0.12 dex. Intermediate S-to-N of R_{23} results in the typical $\sigma_{\log(O/H)} = 0.05 - 0.06$ dex.

Table 3. Observed nearby void dwarfs and new O/H data

No.	Name	J2000 Coord	V_{orig} km s ⁻¹	V_{SALT} km s ⁻¹	D_{\dagger} Mpc	B_t mag	M_B mag	12+log(O/H) ±err.	Notes
1	2	3	4	5	6	7	8	9	10
1	J0015+0104	J001520.7+010437	2055±02	2141±15	28.8	18.31	-14.32	7.14±0.04 d+s	prototype XMP
2	ESO294-010	J002633.4-415120	113±04	84±20	†2.0	15.56	-10.90	7.79±0.12 mse	
3	PGC004055	J010822.0-381233	654±60	633±10	6.8	16.09	-13.09	7.60±0.10 mse+d	
4	UGC01085	J013118.9+074716	652±02	680±07	10.0	16.75	-13.44	7.87±0.11 mse	
5	AGC124137*	J023137.0+093144	897±06	900±10	14.0	17.98	-12.10	7.20±0.12 s+mse	low S-to-N
6	ESO199-007	J025804.1-492256	630±05	623±15	†6.0	16.50	-12.49	7.33±0.06 s	aver. on 2 knots
7	PGC1166738*	J030646.9+002811	710±04	728±20	11.0	18.41	-12.27	7.19±0.04 s	aver. on 2 knots
8	PGC013294*	J033556.8-451129	737±42	750±10	†7.3	16.07	-13.29	7.90±0.06 d	
9	PGC712531	J033903.0-304921	839±123	692±10	9.5	18.29	-11.96	...	only faint H α
10	PGC681755	J033955.0-330309	747±26	705±15	9.5	16.55	-13.39	7.71±0.11: mse	low O ₃₂ ~0.25
11	ESO359-024	J041057.5-354951	847±05	815±30	10.9	15.43	-14.80	7.44±0.13 d	
12	PGC016389	J045658.7-424802	662±06	710±12	†7.0	14.46	-14.80	7.20±0.05 s	~7.0 in O ₃₂ ~0.2
13	HIPASSJ0517-32	J051721.6-324535	798±06	811±06	10.7	15.96	-14.81	7.93±0.05 d	aver. 2 knots
14	ESO553-046	J052705.8-204040	542±06	538±05	†6.7	14.72	-14.71	8.03±0.03 d	
15	PGC138836	J055735.2+072913	428±04	407±15	†5.5	18.40	-11.28	7.56±0.10 mse	
16	PGC018431	J060719.7-341216	774±13	816±07	†9.6	15.66	-14.34	7.65±0.06 d	aver. 2 knots
17	ESO308-022	J063932.9-404317	822±04	888±11	†9.4	16.22	-14.03	7.34±0.05 s	
18	PGC020125	J070517.7-583108	564±04	489±05	†5.3	14.95	-14.16	7.37±0.05 s	aver. 2 knots
19	6dFJ0935-1348	J093521.6-134852	800±44	877±22	11.7	16.43	-14.10	7.28±0.07 s	
20	PGC029033	J100138.2-081455	446±03	258±28	7.0	15.41	-14.07	8.01±0.15 mse	V(HI)-V(opt)~190
21	PGC041667	J123307.9-003158	740±09	737±37	10.2	16.50	-13.63	7.84±0.14 mse	
22	PGC091215	J123655.0+013654	590±01	623±12	6.1	16.35	-12.65	7.37±0.05 s	aver. on 3 knots
23	AGC227970	J124601.4+042252	643±04	625±10	9.2	16.00	-13.93	7.71±0.08 d	
24	AGC225197	J124942.1+052922	739±18	820±30	10.1	18.38	-11.77	...	abs. spectrum
25	UGC07983	J124947.0+035033	694±02	743±20	10.1	16.11	-14.08	8.03±0.14 mse	
26	PGC1289726	J124959.2+054916	618±01	600±10	9.1	16.76	-13.17	7.68±0.11 mse	
27	AGC227972	J125024.0+045422	650±04	647±20	9.1	19.50	-10.46	...	only H α in 2 knots
28	AGC227973	J125039.9+052052	675±04	695±15	9.1	19.50	-10.42	7.07±0.04 s	aver. on 2 measur.
29	AGC226122	J125215.4+042727	700±04	756±15	10.0	18.33	-11.86	...	only H α
30	PGC1264260	J125343.3+040914	761±01	810±12	10.0	17.45	-12.69	7.58±0.08 d	
31	UGC08055	J125604.4+034846	616±02	622±18	6.7	15.94	-13.34	7.79±0.11 mse	
32	PGC044681*	J125956.6-192441	827±02	796±15	†7.3	17.00	-12.73	7.34±0.08 s	check earlier data
33	KKH86	J135433.4+041440	286±02	298±30	†2.6	17.08	-10.14	...	only Bal. absorb.
34	AGC716018*	J143048.7+070926	1365±04	1415±12	18.1	18.18	-13.22	7.93±0.14 mse	
35	AGC249197*	J144950.7+095630	1809±05	1822±10	24.2	18.69	-13.35	7.39±0.06 s	
36	HIPASSJ1738-57*	J173842.9-571525	858±08	815±13	7.3	16.62	-13.12	7.72±0.11 mse	7.77±0.18 (d)
37	PGC408791	J202608.8-552950	893±67	812±10	6.8	16.88	-12.71	7.39±0.05 s	
38	PGC129680	J210804.8-471942	860±33	858±12	7.7	15.69	-13.90	8.00±0.10 mse	aver. 2 knots
39	PGC1016598*	J213902.9-073443	1283±02	1305±12	15.4	18.63	-12.43	7.23±0.04 s	aver. 2 knots
40	ESO289-020	J222111.7-454035	912±67	892±06	8.8	15.62	-14.17	7.59±0.05 mse	aver. 3 knots
41	ESO238-005*	J222230.5-482414	706±03	714±04	†8.0	15.30	-14.28	7.35±0.04 s	
42	PGC1028063	J224223.4-065010	899±06	861±06	10.7	16.02	-14.28	7.79±0.09 d	
43	ESO347-017	J232656.2-372049	691±03	698±06	6.5	14.93	-14.20	7.82±0.03 d	aver. 3 knots
44	PGC3192333	J234133.8-353023	630±89	524±18	6.6	18.86	-10.31	7.26±0.08 d	7.18±0.05 (s)
45	PGC680341	J234147.5-330841	510±89	446±10	4.4	16.59	-11.69	7.34±0.04 d	7.29±0.04 (s)
46	ESO348-009	J234923.4-374622	647±02	587±15	6.1	14.81	-14.18	7.42±0.05 s	
47	ESO149-003	J235202.8-523438	574±04	526±09	†7.0	15.09	-14.20	7.66±0.03 d	

Table 3 content is described in detail in Sect. 4.1. Here we give the brief information. Col. 2: target name from NVG. Col. 3: galaxy coordinates adopted from NVG. Col. 4: original radial velocity with its error, in km s⁻¹. Col. 5: SALT radial velocity with its error; Columns 6, 7 and 8: the adopted distance, total blue magnitude and absolute blue magnitude. Col. 9: derived O/H as 12+log(O/H) and its error, in dex, with indication of the method used: (d) – the direct (T_e) method; (mse) – the modified semi-empirical method of Izotov & Thuan (2007), accounting for the large range of excitation (Pustilnik et al. 2021); (s) – the new empirical strong line O/H estimator of Izotov et al. (2019), with subtracted 0.01 dex to account for a small offset relative to O/H(T_e). In Col. 10 we show brief notes with more detailed information, when necessary, presented in Sec. 4.1.1, 4.1.2. * - from list of 60 XMP candidate in PEPK20; † marks velocity-independent distances obtained with the TRGB method at HST.

Table 4. SALT results for objects with wrong velocities

No.	Name	J2000 coord.	V_{orig} km s ⁻¹	V_{SALT} km s ⁻¹	B-mag	M_B	Notes
1	2	3	4	5	6	7	8
1	PGC3197756†	J001736.3–312618	749±123	2703±10	19.28	-13.64	doubtful, too narrow H α
2	PGC901638	J002951.4–160954	724±59	$z = 0.092$	17.74	-20.30	abs. spectrum
3	PGC3207684	J020140.1–291749	660±123	$z = 0.109$	19.45	-18.90	
4	PGC3210819	J022308.8–295233	779±89	$z = 0.16274$	18.85	-20.30	
5	PGC504827†	J024024.4–471257	812±29	1828±15	19.24	-12.68	only faint H α
6	PGC645417†	J032733.9–354303	723±79	9942±20	16.84	-18.86	only H α
7	PGC016383	J045701.2–424803	3443±61	2953±10	15.48	-17.30	on slit with PGC016389
8	AGC208329	J101531.9+033508	1018±04	1370±10	19.42	-12.1:	12+log(O/H)(mse)=7.82. see text
9	[MU2012]J1355+04B	J135429.5+041237	...	4831±9	19.5:	-14.6:	12+log(O/H)(mse)=7.56. see text
10	PGC1069207†	J143011.3–033552	690±123	988±9	18.34	-12.50	New D = 12.2 Mpc
11	PGC264615	J161354.9–721446	383±11	$z = 0.0695$	17.94	-19.3	LINER?
12	PGC064718	J202733.8–550525	831±52	10710±35	15.24	-21.2
13	PGC162688	J204847.3–121654	843±45	5860±12	17.12	-17.6:
14	PGC163318†	J213935.2–401653	1034±59	$z = 0.0645$	17.25	-19.95	with close E-gal at $z = 0.0630$
15	6dFJ2226336-291728	J222633.6–291728	1025±45	$z = 0.315$	19.57	-21.0:	AGN Sy1.5
16	ABELL3888.14:[PSE2006]1816	J223329.3–372731	1008±19	-166±10	18.49	...	star-like
17	ABELL3888.12:[PSE2006]2246	J223633.3–373005	760±13	$z = 0.388$	18.80	-22.3:	star-like

 † grism PG2300, range ~ 6060 – 6880 Å

4 RESULTS OF SPECTRAL OBSERVATIONS AND O/H ESTIMATES

4.1 Void galaxies

The 1D SALT spectra of the observed void dwarfs are presented in the on-line supplementary materials in Appendix B, Figs. B1–B4. The measured fluxes of emission lines and their derivatives: EW(abs) – the adopted equivalent width of Balmer absorption in the underlying stellar continuum, the extinction coefficient $C(H\beta)$, and the equivalent width of the $H\beta$ emission line $EW(H\beta)$ are presented in Tables C1–C14 of the on-line supplementary materials in Appendix C. Some of the obtained spectra, show rather strong Balmer absorptions in the UV. In these cases the underlying continuum and Balmer absorptions were fitted by a model with the ULYSS package (<http://ulyss.univ-lyon1.fr>, Koleva et al. 2009). This model model spectrum corrected the flux of $H\beta$ emission to a first approximation. In these cases, the EW(abs) derived with the procedure from Izotov et al. (1994) at the next step, appears the residual EW(abs), since this is mainly accounted for by the ULYSS fitting. As mentioned in Section 2, the absolute flux calibration at SALT is rather uncertain. Therefore, we do not provide the absolute flux in the emission $H\beta$.

The derived physical parameters — T_e in the zones of emission of [OIII] and [OII], the relative numbers of ions O^+ , O^{++} and the total abundance of Oxygen relative to Hydrogen, O/H — are shown in the bottom of these tables. As described in Section 3, $T_e(O^{++})$ is calculated with the direct method when the faint auroral line [OIII] $\lambda 4363$ is detected. In the remaining cases it is estimated with the modified semi-empirical method from Pustilnik et al. (2021), based on the semi-empirical method of Izotov & Thuan (2007).

As explained in that section, $T_e(O^+)$ was calculated via the relation (2), adopted from Izotov et al. (1994).

Since the [SiII] $\lambda\lambda 6717, 6731$ was outside the range of SALT spectra, the estimate of electron density N_e in the observed HII regions was impossible. We adopted for further calculations of O/H in the direct and mse methods $N_e = 10 \text{ cm}^{-3}$ as a typical value for HII regions in the low-mass late-type galaxies.

For each galaxy, we present the derived parameter 12+log(O/H). For majority of the obtained spectra, this is derived either with the direct method (for the twelve objects, where it is applicable), or with the empirical strong-line method of Izotov et al. (2019) (for 15 the lowest O/H objects). For the remaining 12 objects, with the higher values of O/H, we apply a modified semi-empirical (mse) method, in which we account for the dependence of the empirically derived T_e on the excitation parameter O_{32} (see details in Pustilnik et al. 2021).

We note that 12+log(O/H), derived with the mse method, needs a small correction (up to 0.03 dex, depending on the value of O/H) in order to make its zero-points consistent with that for the direct T_e method. See Appendix in Pustilnik et al. (2021) for details. This correction is already applied in Tables C1–C15 and the respective value of O/H is indicated as (mse,c). It is reasonable to add a caution on the applicability of mse method for the lowest excitation HII regions. As discussed in the Appendix of Pustilnik et al. (2021), the fitting formulae for deriving T_e via this method, are limited by the lower values of parameter O_{32} . For the range of 12+log(O/H) > 7.5 dex, this lower limit of O_{32} is ~ 0.4 , while for the range of 12+log(O/H) < 7.5 dex, this limit is ~ 0.5 . For several our galaxies with the lowest excitation, the used formulae are slightly extrapolated outside

these limits. For these objects, the uncertainty of the derived value of $12+\log(\text{O}/\text{H})$ can be somewhat underestimated.

Finally, where it is suitable, just to demonstrate the consistency of our estimates with other popular methods, we provide the value of O/H , derived with the empirical estimator of Pilyugin & Thuan (2005) (lower branch), which is based only on the flux ratios of the strong Oxygen lines. Their formulae also account for parameter of excitation O_{32} , which enters to their parameter 'P'. Their formulae are obtained via the fitting of the observational data for HII regions with the direct value of $12+\log(\text{O}/\text{H})$. However, the applicability of their formulae is limited by the range of parameter 'P' of 0.55 and 0.97. This translates to the range of O_{32} of 0.92 to 24.2. Therefore, for our galaxies with the lowest values of O_{32} , we do not show values of O/H (PT05) due to their systematic shifts.

In Table 3 we summarise the adopted parameter $12+\log(\text{O}/\text{H})$ and provide some other parameters of the studied galaxies. The content of the column is as follows: Col. 1 – the number of galaxy, as it appears in Table 1; Col. 2 – the galaxy name as adopted in the NVG catalog, which, in turn, is mainly from the HyperLEDA database³; Col. 3 – J2000 epoch coordinates; Col. 4 – the original heliocentric velocity with the cited error, in km s^{-1} ; Col. 5 – the heliocentric velocity with its error obtained from our SALT spectra; Col. 6 – Distance in Mpc. For 13 galaxies this is measured with the Tip of RGB (TRGB) method. For the remaining objects, the peculiar velocity correction is used according to the velocity field from Tully et al. (2008) as also adopted in the Nearby Void Galaxies catalog (PTM19); Col. 7 – an estimate of the total B -band magnitude; Col. 8 – the absolute magnitude M_B , with the adopted MW extinction correction from Schlafly & Finkbeiner (2011); Col. 9 – the value of $12+\log(\text{O}/\text{H})$, its $1-\sigma$ uncertainty and the method used; Col. 10 – notes for some of the program objects.

In total, we observed on both programs 47 objects belonging to the NVG (Nearby Void Galaxy) sample. Also, we observed 15 more galaxies, adopted in the NVG catalog to reside in the nearby voids. This was done based on their HyperLEDA radial velocities. On results of our spectroscopy, they appeared to be not the NVG objects. Two more galaxies were observed in order to check their radial velocities. One was a potential companion of the void galaxy KKH86, while another galaxy was in a visual contact with the void galaxy PGC16389. We devote to these 17 objects Sect. 4.3.

Nine galaxies (of them, eight – new) were observed as a continuation of the two previous papers to search for XMP dwarfs (Pustilnik et al. 2020b, 2021) among the 60 preselected void XMP candidates (Pustilnik et al. 2020a). Accounting for results on 46 already published objects from this program and several remaining galaxies in the Northern hemisphere, observed at BTA, the program is very close to its completion.

4.1.1 Comments on the most metal-poor galaxies

SDSS J0015+0104 = AGC103435. This galaxy, residing in the Eridanus void (Pustilnik et al. 2013; Kniazev et al. 2018), appeared as an XMP object in two papers, with

the values of $12+\log(\text{O}/\text{H})$ from 7.07 ± 0.06 to 7.03 dex (Guseva et al. 2009; Izotov et al. 2019). This galaxy is one of the prototype objects for the search for void XMP dwarfs. Therefore, it was important to improve its O/H accuracy. The line $[\text{OII}]\lambda 3727$ was either outside the available spectral range (Izotov et al. 2019), or the original semi-empirical method was used (Izotov & Thuan 2007) for too low excitation parameter O_{32} of ~ 0.5 (Guseva et al. 2009). Our spectrum is quite similar to that of Guseva et al. (2009), with a higher S-to-N ratio, since we have even marginally detected a faint $[\text{OIII}]\lambda 4363$. The main difference with their spectrum is our factor ~ 1.2 larger relative fluxes of $[\text{OII}]\lambda 3727$ and $[\text{OIII}]\lambda 5007$.

AGC124137 = J023137.0+093144. This new XMP dwarf was originally selected as a candidate XMP object in Pustilnik et al. (2020a). The emission lines of the only compact knot are faint and overlay on the underlying blue continuum with the Balmer-line absorptions. In Figure B1 we show both, the original spectrum (black) and the result of the subtraction of the SSP model spectrum (blue) after the ULYSS package application. While the S-to-N in the used lines for the strong-line and mse methods is quite low, both methods give the consistent O/H estimates. Since the uncertainty of the measured flux of $\text{H}\gamma$ is large, we varied it in order to check its effect on the derived $\text{C}(\text{H}\beta)$ and $\text{EW}(\text{abs})$ and on the value of O/H . While the $\text{C}(\text{H}\beta)$ varied from 0.32 up to 0.66–0.69, the respective estimates of $12+\log(\text{O}/\text{H})$ (s) varied from 7.08 to 7.30–7.32 dex. The value of $\text{C}(\text{H}\beta)$ related to the Milky Way extinction is 0.13. Therefore, we believe that $\text{C}(\text{H}\beta) = 0.32$, adopted in Table C2, is a more reliable since is a more typical for this type of dwarfs. However, taking into account the low S-to-N of the data, we adopt for this object in Table 3, the value of O/H , which is an average between the two current extreme estimates. The better quality data will be necessary to qualify confidently this dwarf as an XMP void galaxy.

PGC1166738 = J030646.9+002811. This new XMP dwarf was originally selected as a candidate XMP object in Pustilnik et al. (2020a). We show in Table 3 the value of O/H as an average for two knots. For the knot with the extremely low value of $12+\log(\text{O}/\text{H})(\text{s}) = 7.16\pm 0.05$ dex, we provide all data in Table C3. For the second knot, we obtain the value of $12+\log(\text{O}/\text{H})(\text{s}) = 7.22\pm 0.05$ dex.

In the spectrum of this XMP knot, obtained on 2019.09.06, we detected unusual transient emission lines ($\text{H}\beta$, $\text{H}\alpha$, and $[\text{OIII}]\lambda 5007$), which differed in velocity and strength from those observed in the two later dates, in December 2019. Since the available data are too limited, the nature of this transient remains puzzling. Probably, new observations of this knot will uncover a puzzle of this phenomenon.

PGC016389 = J045658.7–424802 = HIPASSJ0457–42. In this blue patchy elongated oval we have on the slit three different HII regions with varying S-to-N emission lines and with substantial contribution of the underlying Balmer absorptions. To correctly subtract this continuum, we modelled it with the ULYSS package as explained in Section 4.1. In Figure B1 (Appendix B, supplementary material) we present the 1d spectrum of the most metal-poor region (a). The respective line fluxes and derived physical parameters for this region are presented in Table C4 (Appendix C, supplementary material). The very

³ <http://leda.univ-lyon1.fr>

low value of $12+\log(\text{O}/\text{H})$ (s) = 6.98 ± 0.05 dex derived with the method of Izotov et al. (2019) is practically insensitive to the adopted value T_e (with the range of 18.2 KK to 26.2 kK, estimated either via semi-empirical method of Izotov & Thuan (2007), or with the modified method (mse) from Pustilnik et al. (2021).

The main problem with this (as well as with $12+\log(\text{O}/\text{H})$ (mse)) estimate, is the very low excitation of this region. The parameter $O_{32} \sim 0.2$ is 2.5 times smaller than its lower boundary for the sample of HII regions with the direct O/H, which is used to derive the empirical relation in Izotov et al. (2019). Therefore, we should treat the derived very low value of O/H with a caution and rather as an indicative one. In two other regions, 'b' and 'c', we derived $12+\log(\text{O}/\text{H})$ (s) of 7.20 ± 0.05 dex and 7.31 ± 0.09 dex, respectively. While for region 'c', O_{32} is very small, of ~ 0.1 , for region 'b', $O_{32} \sim 0.46$. Having all this information in hands, we currently adopt its $12+\log(\text{O}/\text{H})$ (s) = 7.20 ± 0.05 dex. Since the galaxy shows multiple SF regions, we hope that the follow-up high S-to-N spectroscopy will allow one to better determine the range of metallicities in this dwarf.

AGC227973 = J125039.9+052052. This new faint XMP dwarf, with the value of $12+\log(\text{O}/\text{H}) = 7.07$ dex, appears to be one of the lowest metallicity LV dwarfs. It is similar on many parameters to the other void XMP galaxy, the Leoncino dwarf (AGC198691 = J0943+3326) (Hirschauer et al. 2016). They have similar distances and atomic gas masses, very close absolute magnitudes and metallicities and amplitude of HI gas motions. The main difference is the a much higher excitation of HII region in AGC198691 that allows to determine its metallicity via the direct method and to address the issue of the primordial Helium (Aver et al. 2022).

PGC044681 = J125956.6-192441. For this dwarf, we already obtained the SALT spectrum presented in Pustilnik et al. (2020b). For those rather noisy data for the used emission lines, we found its $12+\log(\text{O}/\text{H})(s) = 7.22\pm 0.09$ dex, with the upward correction by 0.02 dex relative to that paper, due to the updated zero-point correction for Izotov et al. (2019) method, as described in Sect. 3. Since that time, a much better quality images of this dwarf appeared in the Legacy surveys and the Hubble Legacy Archive. We use them to select the different slit position for the repeat observation. The new value of $12+\log(\text{O}/\text{H})(s) = 7.34\pm 0.08$ dex, is, from the one hand, marginally consistent with the first measurement. On the other hand, since it probes the other HII region, it does not exclude the lower value for that region.

4.1.2 Comments on the other individual void galaxies

ESO308-022 = J063932.9-404317. The slit was positioned far from the main dwarf galaxy body, on the outer SF region well seen at the HST image. Its radial velocity differs by ~ 60 km s^{-1} from that of the main galaxy derived from its HI emission (Huchtmeier et al. 2000). Since the width of HI profile, $W_{20} \sim 70$ km s^{-1} , one can think that the studied here SF region can belong to ESO308-022, or alternatively, is a smaller gas-rich companion in which the current SF episode was triggered by the tidal interaction with a more massive neighbour. Probably HI mapping

of this galaxy will clear up the nature of this star-forming gas blob.

PGC029033 = J100138.2-081455. For this galaxy, we detected unusually large difference between the HI-line velocity of $V(\text{HI}) = 446\pm 1.5$ km s^{-1} (Huchtmeier et al. 2003) and our emission line velocity $V(\text{opt}) = 258\pm 28$ km s^{-1} for the slit position crossing the W edge of galaxy body. The rotation velocity of the galaxy is rather small as follows from the width of HI profile $W_{0.5} = 49$ km s^{-1} (Huchtmeier et al. 2003). While the optical morphology of this dwarf does not look disturbed, this very large difference in radial velocities of the atomic and ionised gas hints on its non-equilibrium state, probably caused by a recent interaction or a minor merger. The gas metallicity of this dwarf, despite bearing rather large uncertainties, also looks rather enhanced in comparison to the similar luminosity void dwarfs. Also, it is not clear which of the two velocities reflect the systemic velocity of the galaxy, which is used for the distance determination. For the moment, we use the HI-based velocity. So, the more detailed study of HI gas kinematics can shed light on the recent processes in this object.

PGC1016598 = J213902.9-073443. In this galaxy the emission on the slit is splitted onto two close (~ 7 pixels, or ~ 3.5 arcsec, in between) knots (W and E) with quite different flux ratios of $[\text{OIII}]\lambda\lambda 4959, 5007$ lines to $\text{H}\beta$. The half-widths of their extent along the slit are close to the distance between the knots, so that there is a substantial overlapping of their light if we simply extract spectrum of each knot. To obtain the more reliable line strengths in the E and W knots, we undertook a two-gaussian fitting along the slit for all lines of interest. Despite the knots show quite different excitation parameter O_{32} (1.9 versus 0.44), their parameter $12+\log(\text{O}/\text{H})$ (s) is close within rather small uncertainties (7.26 ± 0.05 dex and 7.19 ± 0.06 dex, respectively). Therefore, we adopt their average value, 7.23 ± 0.04 dex.

4.2 Improved velocities and distances for void galaxies

For several void objects from Table 3, the HyperLEDA radial velocities have moderate to low accuracies (60–120 km s^{-1} , or for related distances, ~ 0.9 –1.8 Mpc). For objects in the LV and its environs, this results in the substantial uncertainties in both the relative positions to the nearby neighbours and to their distance-dependent parameters. In Table 3 we give for all objects the distances and related M_B based on NVG (HyperLEDA) data. Here we briefly summarise galaxies, for which we obtained a better accuracy radial velocities.

PGC712531 = J033903.0-304921. V_{hel} changed from 839 to 692 km s^{-1} and the related D – from 10.95 to 9.3 Mpc.

6dFJ0935216-134852. V_{hel} changed from 800 to 877 km s^{-1} and the related D – from 11.7 to 12.7 Mpc.

PGC408791 = J202608.8-552950. V_{hel} changed from 893 to 812 km s^{-1} and the related D – from 7.5 to 6.4 Mpc.

PGC3192333 = J234133.8-353023. V_{hel} changed from 630 to 524 km s^{-1} and the related D – from 6.6 to 5.2 Mpc.

PGC680341 = J234147.5-330841. V_{hel} changed from 510 to 446 km s^{-1} and the related D – from 4.4 to 3.5 Mpc.

4.3 Mistaken objects

In Table 4 we summarise the results of observations for 15 objects, which appeared to have wrong radial velocities in HyperLEDA and/or in the original papers. Due to these errors, they reside far from the distances adopted in the PTM19, and, hence, should be excluded from the NVG sample. The two exceptions in this Table are the galaxies [MU2012]J1355+04B and PGC016383. For the former, the information on its radial velocity was absent. Makarov & Uklein (2012) suggested that this is a fainter companion of the known LV dwarf KKH86. For the latter, its known radial velocity placed the galaxy far outside the distance of 25 Mpc, in which the NVG sample is picked-up. We obtained its independent value just because positioned the long slit at the void galaxy PGC016389 so that it also crossed PGC016383. See Sect. 4.3.1.

We show 1D spectra of all these objects in the on-line supplementary materials in Appendix B, Fig. B5–B6 and present the related data in Table 4. The Table includes the following information. Column 2 - the name of the object adopted from HyperLEDA. Column 3 - its J2000 coordinates. Column 4 - the original heliocentric velocity from HyperLEDA used to assign the object to the NVG sample. Column 5 - the heliocentric velocity on the results of the SALT spectroscopy. For seven very distant objects we give their redshifts instead of radial velocity. Column 6 - B-band magnitude adopted from HyperLEDA. Column 7 - estimated absolute B-band magnitude based on parameters in Columns 5 and 6. Column 8 - brief notes. For several objects, we present below more detailed comments.

4.3.1 Comments on individual mistaken objects

PGC016383=J045701.2–424803. This known background galaxy looks to be in contact with the unrelated void galaxy PGC016389 from Table 3. The SALT slit was positioned to cross both galaxies. We did not expect to find something new. However, the E+A spectrum of PGC016383 shows the radial velocity of $V_{\text{hel}} = 2953 \text{ km s}^{-1}$, about 500 km s^{-1} smaller than the adopted value in HyperLEDA.

AGC208329 and SDSSJ101531.9+033508. This blue irregular galaxy is identified in ALFALFA (Haynes et al. 2018) with HI-source at position J101528.4+033544 with the catalog velocity $V_{\text{hel,HI}} = 1018 \pm 2 \text{ km s}^{-1}$. The velocity determined on two HII-regions, $V_{\text{hel,opt}} \sim 1370 \text{ km s}^{-1}$, drastically differs from that $V_{\text{hel,HI}}$. Due to this inconsistency, we have checked the original data of this HI-source as presented in the ALFALFA database. Indeed, there is a rather strong source at $V_{\text{hel,HI}} = 1018 \text{ km s}^{-1}$ (Fig. 1). In addition, there is a faint, marginally-detected source with $F(\text{HI}) \sim 0.2 \text{ Jy km s}^{-1}$ at $V_{\text{hel,HI}} \sim 1370 \text{ km s}^{-1}$. We identify this HI source with the star-forming dwarf, for which we obtained the same radial velocity of the ionised gas.

The optical galaxy has no alternative names in HyperLEDA. However, it is identified with two SDSS objects: J101531.88+033508.4 – for its ‘centre’, and J101531.32+033508.9 – for the blue compact knot at the W edge. Both objects were on the SALT slit. They have rather similar spectra and the close radial velocities. This SDSS dwarf is seemingly associated with several dwarf galaxies in the group of the Sa galaxy NGC3169 (J101414.8+032759)

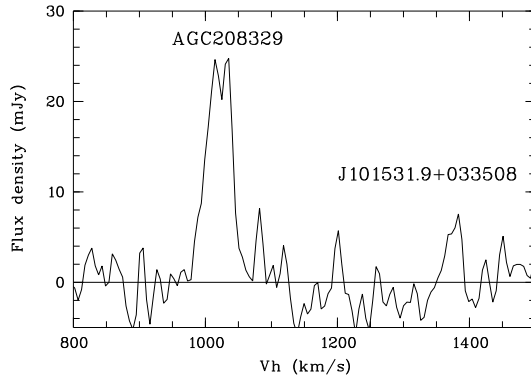


Figure 1. ALFALFA HI profile of AGC208329 at $V_{\text{hel}} = 1018 \text{ km s}^{-1}$ and a fainter object at $V_{\text{hel}} \sim 1370 \text{ km s}^{-1}$. The latter is close to that of the optical velocity of SDSSJ101531.88+033508.4 measured in this work.

with $M_B = -20.6 \text{ mag}$, at $V_{\text{hel}} = 1232 \text{ km s}^{-1}$. Therefore, this optical SDSS object should be excluded from the NVG sample.

As for the nature of AGC208329 itself and an associated with it ‘galaxy’, it remains puzzling, since no other potential optical counterparts are visible in the Legacy surveys colour images within the five-arcmin radius. One can suggest that the optical counterpart of AGC208329 is a very low SB void dwarf which falls close to light sight of a much brighter dwarf SDSSJ101531.88+033508.4, for which we obtained optical spectrum. For the typical ratio of $M(\text{HI})/L_B \sim 1$, for AGC208329 with $F(\text{HI}) = 1.15 \text{ Jy km s}^{-1}$, one expects for its counterpart a galaxy with $B_{\text{tot}} = 16.9 \text{ mag}$, 2.5 mag brighter than that of SDSSJ101531.88+033508.4. To be invisible, this counterpart should be comparable on the total magnitude with this SDSS dwarf (and hence, to be very gas-rich, with $M(\text{HI})/L_B \sim 10$) and to have a much larger angular extent. Probably, the future very deep images of this region will detect such an unusual LSB void dwarf.

[MU2012]J1355+04B = J135429.5+041237. This blue irregular galaxy was suggested by Makarov & Uklein (2012) as a counterpart for a nearby void dwarf KKH86 with $V_{\text{hel}} = 220 \text{ km s}^{-1}$ (see Table 3). Our SALT spectrum shows this is a dwarf ($M_B \sim -14 \text{ mag}$) emission-line galaxy at the $D \sim 66 \text{ Mpc}$. The strong Oxygen lines in its HII region allow one to estimate its Oxygen abundance via the ‘mse’ method described above. This gives the value of $12 + \log(\text{O}/\text{H}) = 7.56 \pm 11 \text{ dex}$.

PGC264615 = J161354.9–721446, not HIPASS J1614-72. This blue galaxy was suggested as an optical counterpart for the faint HI-source HIPASS J1614-72 by Kilborn et al. (2002). It is separated from the Parks radio position (J161422.45-721554.9, with an accuracy of $\sim 1.9 \text{ arcmin}$) by 2.4 arcmin. For the HI radial velocity of $V_{\text{hel}}(\text{HI}) = 383 \text{ km s}^{-1}$, the distance to this object, derived via the kinematical model of Tully et al. (2008), is only $\sim 2.5 \text{ Mpc}$. Hence, this HI-source belongs to a few per cent of the nearest NVG sample galaxies. Due to the poor coverage of this sky region by the imaging surveys, its real optical counterpart is still waiting for identification. PGC264615 itself appears a distant SF galaxy with the redshift of ~ 0.07 . NED

(NASA/IPAC Extragalactic Database) gives a half-dozen galaxies with close redshifts within the radius of 1 degree.

PGC163318=J212935.2–401653. The target galaxy looks like as a small disc with a brighter central core. An off-set red 'star' is situated at ~ 5 arcsec to NE. Both objects on the slit display rather similar spectra, with the prominent absorption features slightly shifted one relative to the other. The non-shifted strong absorption at the edge of the spectrum is the telluric O_2 band at $\approx \lambda 6870 \text{ \AA}$. The other prominent absorption doublet at $\sim \lambda 6270 \text{ \AA}$ shows the shift and thus should be intrinsic for both objects. The most probable identification of this doublet is NaI D1,D2 (5889.95 and 5895.92 \AA) at the redshift of $z = 0.0645$. Then 'red' star appears to be an E-galaxy with the radial velocity $\sim 450 \text{ km s}^{-1}$ lower than that of the target object. The fainter absorption features in the spectra of the both galaxies are well consistent on the wavelengths with the absorption lines visible in spectra of K7-M0 dwarfs from templates in paper by Kesseli et al. (2017). Probably these two galaxies comprise a group with a brighter E galaxy at ~ 30 arcsec to SW.

5 DISCUSSION

As described in the Introduction, this work includes the observational results on the ionised gas metallicity from two different projects: a) the search for new XMP dwarfs among galaxies in the NVG sample, and b) the unbiased study of all void galaxies in the LV, that is about 260 the nearest galaxies of the whole NVG sample of 1354 objects. We summarise the respective results below.

5.1 Search for XMP dwarfs in the NVG sample

Altogether, it was selected 60 NVG sample galaxies with $M_B > -14.3$, which on the other properties were similar to the prototype XMP void dwarfs (Pustilnik et al. 2020a). For 46 of them, the spectral data were obtained either with SALT, or with BTA. The related results were published in Pustilnik et al. (2020b, 2021). In this paper, we present the results of observations for 8 new objects and for one already published dwarf and briefly summarise the preliminary statistics of such unusual dwarfs relative to the more common void galaxy population.

Of the preselected 60 NVG XMP candidates, to date, total 54 are observed and presented in Pustilnik et al. (2020b, 2021) and in this paper. Six more objects remain in the BTA part (paper in preparation). Two of these 60 candidates appeared galaxies with wrong velocities (Pustilnik et al. 2020b). One preselected galaxy appeared too Southern, so that it can not be observed with SALT. Of the remaining 57 NVG objects, for 50 we were able to derive the parameter $12+\log(O/H)$. For 11 of these 50, the parameter $12+\log(O/H)$ appears extremely low, in the range of 6.98 to 7.21 dex. 23 more dwarfs of this *candidate* XMP dwarf sample, have $12+\log(O/H)$ in the range 7.23 – 7.39 dex, that corresponds to the range of $Z_{\odot}/30 \lesssim Z(\text{gas}) < Z_{\odot}/20$. That is ~ 20 percent of that preselected candidates appear XMP galaxies with $Z(\text{gas}) < Z_{\odot}/30$. The additional ~ 40 percent of the preselected objects appear very-metal poor, with $Z_{\odot}/30 < Z(\text{gas}) < Z_{\odot}/20$.

The total number of the *nearby* void XMP dwarfs comprises about 20, including the prototype XMP BCG IZw18 and discovered several decades later, well-known galaxies DDO68, with $12+\log(O/H)$ in the range 6.98 – 7.3 dex (Pustilnik et al. 2005; Izotov & Thuan 2007; Annibali et al. 2019), J0926+3343 with $12+\log(O/H) = 7.12$ dex (Pustilnik et al. 2010), and Leoncino dwarf (J0943+3326), with $12+\log(O/H) = 7.07$ dex (Aver et al. 2022).

In Figure 2, we show how the NVG galaxies, observed as the preselected XMP candidates, sit on the diagram $12+\log(O/H)$ versus M_B . The relation between these parameters was derived by Berg et al. (2012) for the reference sample of the LV late-type galaxies with the well-known O/H and distances. We draw this linear relation and two parallel lines showing the value of the rms scatter of this sample (± 0.15 dex) around the linear regression. The pink dot-dashed line is drawn at the 2 rms distance (that is – 0.3 dex) below the reference linear relation. The galaxies with O/H below this line, deviate systematically downwards from the reference relation.

We use O/H estimates derived with the three different methods, discussed above, depending on the situation. When the auroral line $[OIII]\lambda 4363$ is detectable, we use the direct method (black symbols). Otherwise, we use the strong-line method of Izotov et al. (2019) for the range of $12+\log(O/H) \lesssim 7.5$ dex (green symbols) and the mse (modified semi-empirical) method for the higher O/H (blue symbols). Some systematics between the data, obtained with the different methods of the O/H estimate, are basically due to the selection effects.

The appearance of the faint auroral line $[OIII]\lambda 4363$ correlates with the value of ionisation parameter $\log(U)$ or its proxy, the excitation parameter O_{32} , and metallicity. The former, in turn, are related with the strength of SF 'burst' and its age. Since in the unbiased sample of void galaxies, the probability to catch a young and strong burst is rather small, this translates to the low incidence of $[OIII]\lambda 4363$ -line-detected objects. Similarly, since we apply either the 'strong-line' or 'mse' methods in the ranges of $12+\log(O/H) < 7.5$ or > 7.5 dex, the average values of O/H for these two methods show, by definition, the substantial difference.

5.2 Intermediate results on metallicities of the LV void galaxies

The next steps on the spectroscopy of the NVG dwarfs are conducted in the framework of the on-going project of the unbiased study of all void galaxies in the LV. It also finds new very metal-poor objects albeit less frequently. The smaller incidence of the newly-found XMP dwarfs in this project is a natural consequence of the unbiased character of the study of the whole NVG sample in the LV. This is also a reflection of the relative rarity of XMP objects. In this paper, we add two more LV XMP dwarfs, with $12+\log(O/H) = 7.07$ and 7.20 dex, and 7 new dwarfs with $12+\log(O/H) \lesssim 7.39$ dex. A couple of new XMP dwarfs within the LV, which were not preselected as the mentioned above XMP candidates, were also found at the Northern hemisphere with BTA (paper in preparation).

The unbiased approach in the study of void objects allows one to address their diversity, including the scatter of gas metallicity for the similar global parameters, such as

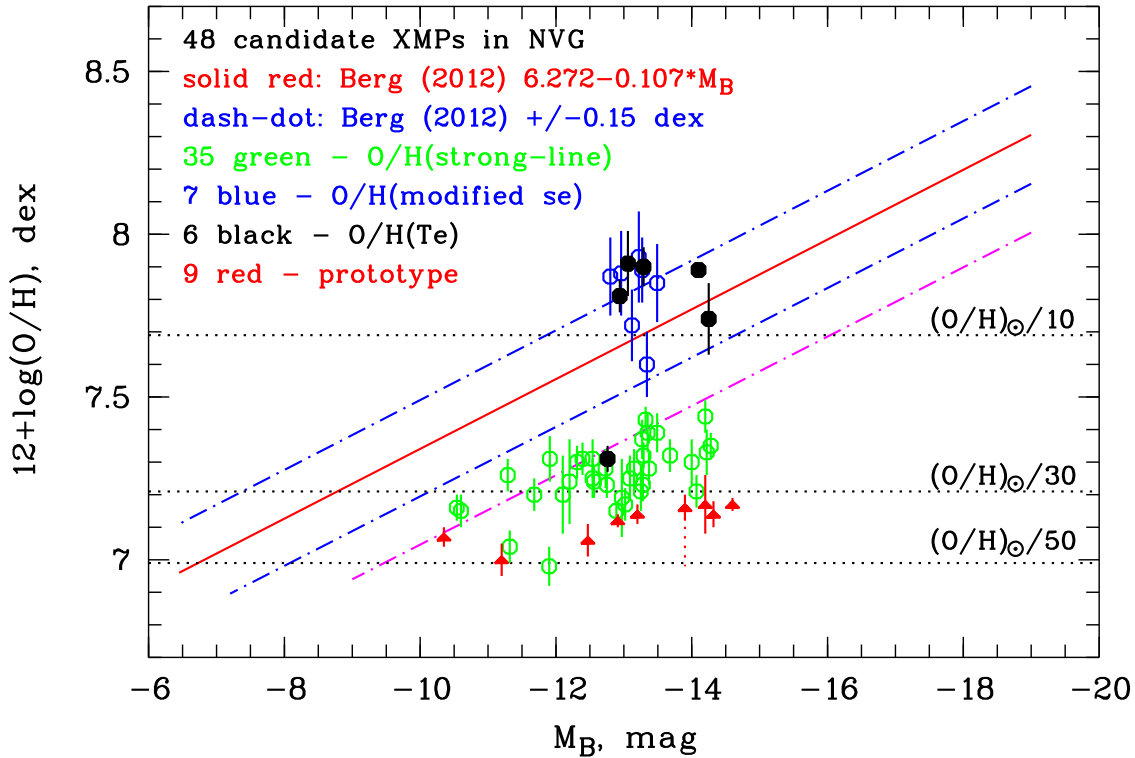


Figure 2. Positions of 48 void dwarfs from NVG galaxies selected in PEPK20 as candidate XMP galaxies. The solid red line is the reference relation derived for a sample of the LV late-type galaxies by Berg et al. (2012). Two blue dash-dotted lines at ± 0.15 dex show the rms scatter of the reference sample. Magenta dash-dotted line runs at -0.30 dex (-2 rms) from the reference relation. Nine prototype objects (red triangles) are known from the earlier studies of XMP void dwarfs summarised in PEPK20. Five of them have O/H determined with the direct method, while the rest four – with the strong-line method of Izotov et al. (2019). The vertical dashed line at $M_B \sim -14.0$ shows the range of O/H for DDO68 from Annibali et al. (2019).

luminosity or stellar mass. To date, we collected data on the gas metallicity in the LV void galaxies for about a hundred objects. They include both, our own results from this paper, some of the LV objects appeared in the other our published samples, as well as about two dozen objects with known O/H, found in the literature. Despite this number comprises less than a half of the whole LV void sample (the updated number of 243 objects), it is useful to have a first look on the available data.

For discussion of the intermediate results on the LV sample, we take at the moment only the data with the direct and strong-line O/H estimates. The mse estimates of O/H from this and the previous papers will be included in the next publication, along with the earlier data. The latter need a more careful reanalysis, including those where we used the semi-empirical method of Izotov & Thuan (2007).

The plot with the intermediate results for the LV void sample is presented in Figure 3. The lines for the reference sample are the same as in Figure 2.

One of the features, which distinguishes this void galaxies sample from, e.g., the sample of Lynx-Cancer void, is its heterogeneity in the context of their distances to the nearest massive galaxies. As described in PTM19, the NVG galaxy

sample was selected of objects falling within the empty spheres comprising the voids themselves. About 20 per cent of this way selected galaxies appeared to reside closer than two Mpc to the bordering massive galaxies. They were conditionally named outer void galaxies, while the great majority of galaxies (~ 80 per cent) with the D_{NN} (nearby luminous neighbour) distances larger than 2 Mpc were assigned to the inner void galaxies.

As one can see in Figure 3, the scatter of the LV void galaxies (filled and empty octagons with error bars) on $\log(O/H)$ at a fixed M_B , appears significantly larger than for the reference sample of Berg et al. (2012). For the latter sample, the scatter is mostly limited by the blue dot-dashed parallel lines (± 1 rms scatter). While the sizeable part of void galaxies falls within the $\log(O/H)$ range of the reference sample, about one third of the void objects have a substantially reduced metallicity. In particular, in Figure 4 one can see that 28 of 90 LV void galaxies have the $\log(O/H)$, reduced by more than 0.30 dex (two rms) relative to their values expected from the reference relation of Berg et al. (2012).

The majority of void objects with the substantially reduced metallicity in Figure 3 belong to galaxies with

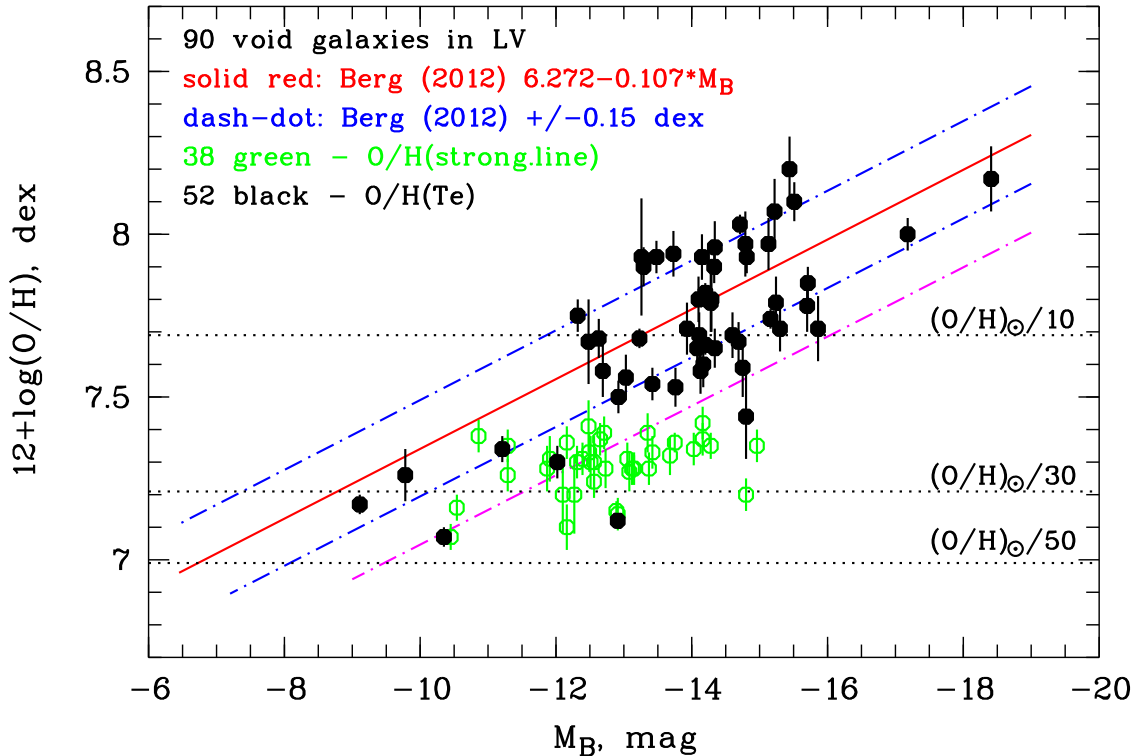


Figure 3. Distribution in the diagram ‘ $12+\log(\text{O}/\text{H})$ vs M_B ’ of the 90 LV void galaxies with known O/H, derived either by the direct (T_e), or by the ‘strong-line’ (Izotov et al. 2019) methods. The lines on the plot are the same as in Figure 2. The data include results from this paper (25 objects) and from our published papers Pustilnik et al. (2016, 2020b, 2021) (31 objects), as well as 12 unpublished BTA objects and 22 objects from the literature (Izotov et al. 1994, 1997; Izotov & Thuan 2007; Izotov et al. 2012; van Zee 1997; van Zee & Haynes 2006; van Zee et al. 2006; Pustilnik et al. 2003; Kniazev et al. 2005; Berg et al. 2012; Skillman et al. 2013).

very low O/H, namely with $12+\log(\text{O}/\text{H}) \lesssim 7.4$. Of them, the great majority have values of O/H derived with the strong-line method of Izotov et al. (2019). In Figure 4 we show histograms of the difference $12+\log(\text{O}/\text{H})(\text{observed}) - 12+\log(\text{O}/\text{H})(\text{reference}, M_B)$, separately for O/H obtained by the direct method (black) and O/H, derived with the strong-line method of Izotov et al. (2019) (green). The mean difference for O/H(T_e) is -0.049 dex, with $\text{rms}=0.175$ dex. For O/H(s), the mean is -0.346 dex, with $\text{rms}=0.116$ dex.

The effect of the reduced metallicity in void galaxies, already mentioned in several our papers, and its elevated scatter for a given galaxy luminosity/mass, can be due to the interplay between various factors. In particular, the chemical evolution of void galaxies and their current metallicity can depend on their local environment and clustering, and on the faster or slower accretion of the unprocessed intergalactic gas. Since void substructure resembles that of a mini-Universe (Gottlöber et al. 2003; Aragon-Calvo & Szalay 2013), void galaxies can be associated with more massive hosts or to be well isolated. In general, the local environment is expected to affect the secular evolution, especially of the smaller-mass companions. To uncover these factors, it takes a more careful analysis of the studied sample.

On the other hand, since we study the LV void galaxy

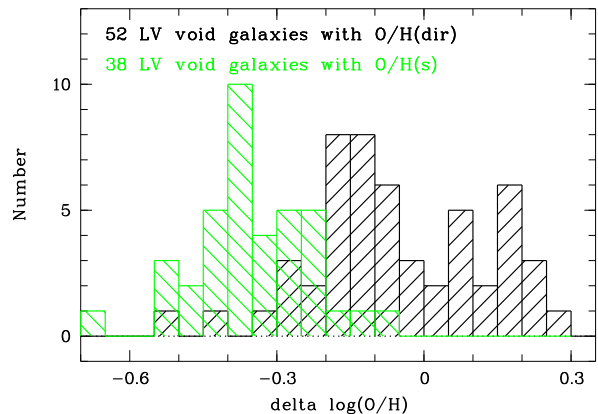


Figure 4. The same data as in Figure 3. The histograms show the differences of measured $12+\log(\text{O}/\text{H})$ for the LV void galaxies and those expected from the reference relation from Berg et al. (2012). Black hatched histogram is for O/H(T_e), while the green histogram is for O/H derived with the strong-line method of Izotov et al. (2019).

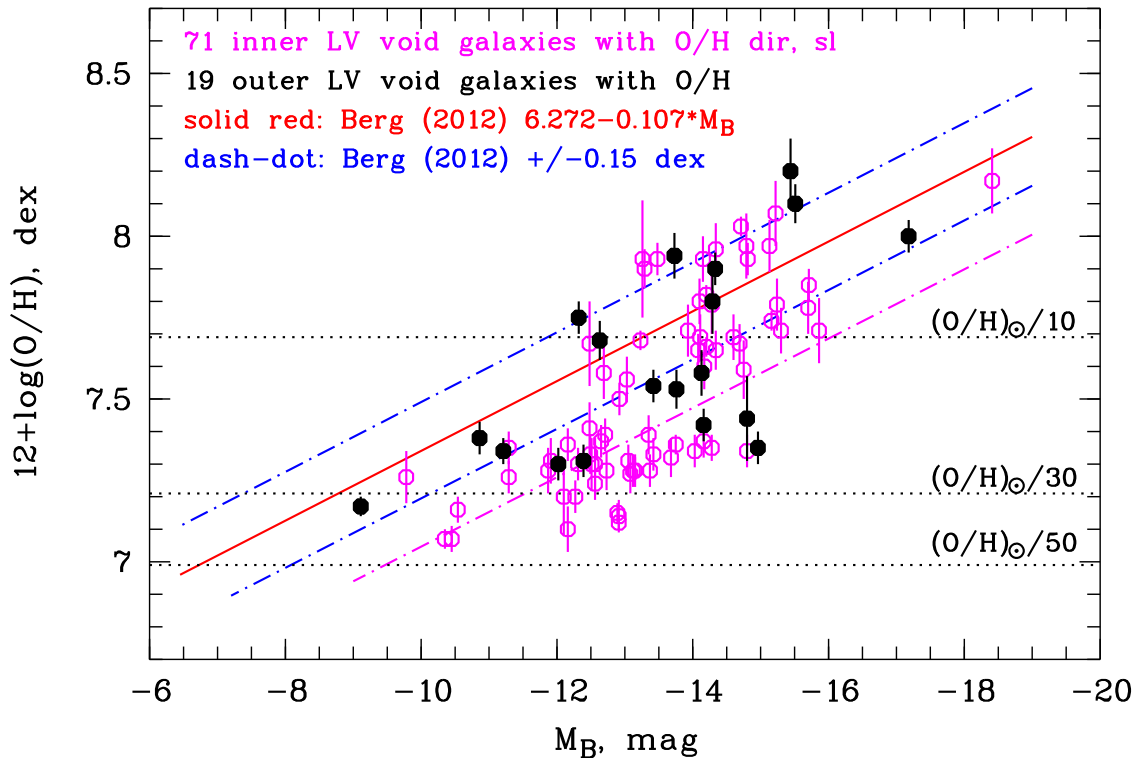


Figure 5. The same data as in the previous figure, but divided according to their distribution within voids. 19 ‘outer’ void galaxies are shown in black. 71 ‘inner’ void galaxies are coloured with magenta. See a more detailed discussion in the text.

sample without any additional bias, we can, in particular, examine, whether the outer and inner void galaxies show differences in their properties. For this, we show outer and inner galaxies in the similar plot in Figure 5. While the statistics is still rather limited, there is a hint that the ‘outer’ void objects show a smaller scatter in $\log(\text{O}/\text{H})$ and follow closer the reference relation of Berg et al. (2012). While the criterion of separation of outer void subsample by the inequality of $D_{\text{NN}} < 2$ Mpc, is somewhat arbitrary, it seems to catch a transition of galaxy properties from the most rarefied regions to a denser environment. Therefore, one can think that the large scatter of void galaxies on $\log(\text{O}/\text{H})$ in Figure 3 can be partly explained by the contribution of the outer objects.

In Figure 6, we show the distribution of differences in $\log(\text{O}/\text{H})$ for 90 LV void galaxies, separately for the ‘inner’ (black) and ‘outer’ (green) subsamples. The left-hand panel shows the histograms for the threshold $D_{\text{NN}} = 2.0$ Mpc, as adopted in the original paper on the NVG sample. The mean for the 71 ‘inner’ galaxies is -0.193 dex with $\text{rms}=0.202$ dex. For the 19 ‘outer’ galaxies, the mean is -0.098 dex, with the $\text{rms}=0.222$ dex. While the scatter for both groups is similar, the ‘inner’ group has a substantially more reduced O/H.

To check, how this effect depends on the adopted threshold for D_{NN} , we divided these 90 LV void galaxies into the ‘inner’ and ‘outer’ subsamples, taking the threshold $D_{\text{NN}} = 1.7$ Mpc. This means that the selected ‘outer’ void galaxies are in average somewhat closer to the bordering large

galaxies. The histograms in the right-hand panel show the difference of $\log(\text{O}/\text{H})$ for this case. For the 78 ‘inner’ galaxies, the mean is -0.191 dex with $\text{rms}=0.204$ dex, practically the same as for the previous histogram. For the 12 ‘outer’ galaxies, the mean is -0.055 dex, with $\text{rms}=0.208$ dex. That is, void galaxies with the smaller D_{NN} show the tendency to have the smaller difference of O/H with the reference relation, albeit the scatter is larger than 0.15 dex characteristic of the reference sample of Berg et al. (2012). We notice that the statistics is still limited, so the future data, incorporating the majority of the LV void galaxies, hopefully will result in more firm conclusions.

5.3 New dTr galaxies in void environment

Several studied void galaxies appear on their properties similar to the handful known voids dwarfs of transitional type (dTr) (Karachentsev et al. 2014; Pustilnik et al. 2022a, and references therein). They show very little current SF as evidenced either by non-detected $\text{H}\alpha$ emission, or a single region with the faint $\text{H}\alpha$. At the same time, their HI content does not differ much from dIr galaxies of the same luminosity. The unbiased study of the LV void dwarfs allows one to extend the sample of these rare objects and to address the issue of their origin on the larger statistical data.

Below we enumerate the void galaxies, according to the

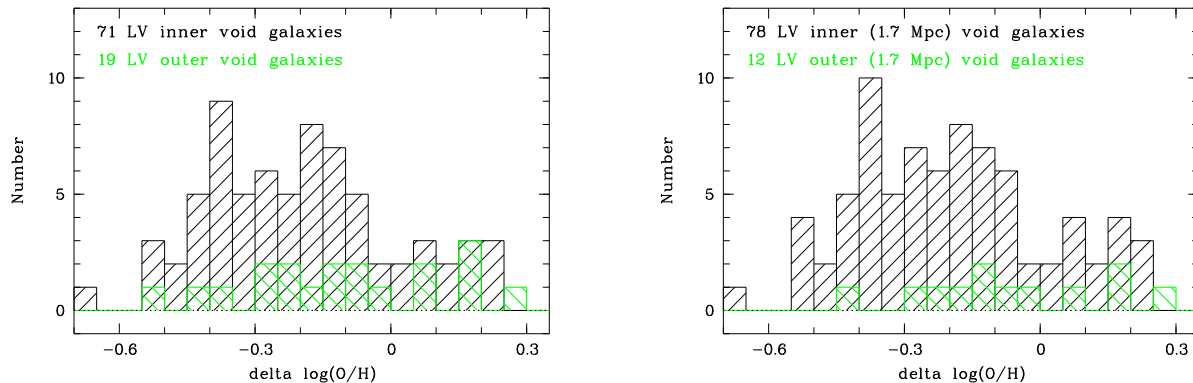


Figure 6. The same data as in Figure 5. The histograms show the differences of measured $12+\log(\text{O}/\text{H})$ for the LV void galaxies and those expected from the reference relation from Berg et al. (2012). **left-hand panel:** separate histograms for ‘inner’ (71 galaxies, black) and ‘outer’ (19 galaxies, green) subsamples for the case of the threshold $D_{\text{NN}} = 2.0$ Mpc. **right-hand panel:** same as the left-hand panel, but for the case of the threshold $D_{\text{NN}} = 1.7$ Mpc. Black histogram is for 78 ‘inner’, while the green one – for 12 ‘outer’ galaxies. See text for more detail.

new data, falling into this category with the higher or lower confidence. Several of them are found as HI-sources in the blind ALFALFA survey (Haynes et al. 2018). A few similar ALFALFA galaxies are found in the SHIELD project described by Cannon et al. (2011); Hauberg et al. (2015); McQuinn et al. (2014).

PGC712531 = J033903.0-304921. This bluish dwarf shows only a faint $\text{H}\alpha$ in emission.

AGC225197 = EVCC1184 = J124942.11+052922. A blue low-surface brightness (LSB) dwarf with the non-central blue compact object. The long slit was positioned to this blue object. Spectrum of this galaxy in SDSS DR12 (Alam et al. 2015) looks similar to our.

AGC227972 - J125024.0+045422. A bluish oval galaxy without prominent SF regions.

PGC2807150 = KKH86 = AGC231980. This LSB dwarf is rather bright HI source, with $F(\text{HI})$ (ALFALFA) = 0.8 Jy km s^{-1} and the ratio of $M(\text{HI})/L_{\text{B}} \sim 0.75$. At the same time, the on-line database of Karachentsev et al. (2013) provides its $\text{H}\alpha$ -net image with no tracers of emission. Our value of its $V_{\text{hel}} = 298 \pm 40 \text{ km s}^{-1}$ comes from the wavelengths of the Balmer absorption lines in the body.

5.4 Issue of mistaken redshifts in the NVG sample

As noticed in the Introduction, the great majority of the NVG sample galaxies in PTM19 are taken from the HyperLEDA data base. On results of our spectral observations of a hundred NVG galaxies (that is residing in the nearby voids), presented in Pustilnik et al. (2020b, 2021) and in this work, we found that ~ 15 per cent of them have velocities different from the catalog (HyperLEDA) values much larger than one expects from the cited uncertainties. The great majority of them comes from objects in the Southern hemisphere. Of these, the majority of objects with wrong velocities appear in the HyperLEDA from the 2dFGRS galaxies with redshifts derived via absorption lines.

This allows us to formulate a caution for the use of the

2dFGRS redshift data for statistical studies of galaxies, at least in the nearby Universe, where we have checked many of their radial velocities.

6 SUMMARY AND CONCLUSIONS

In the previous papers (Pustilnik et al. 2020b, 2021) we presented results of spectroscopy for 46 objects from the sample of 60 preselected *candidate* XMP void objects from the fainter part ($M_{\text{B}} \gtrsim -14.3$) of the Nearby Void Galaxies (NVG) sample. Ten of them were found to be the XMP objects, that is having $12+\log(\text{O}/\text{H}) \lesssim 7.21$ dex. 13 more new void galaxies were found somewhat less metal-poor, with $12+\log(\text{O}/\text{H}) \lesssim 7.35$ dex.

In this work we observed 8 galaxies of the remaining 13 XMP candidates and reobserved one XMP dwarf from Pustilnik et al. (2020b). Two new XMP dwarfs are found of these eight objects. Two additional dwarf galaxies with the Oxygen abundance of $12+\log(\text{O}/\text{H}) \lesssim 7.35$ dex are found as well. Two known XMP void dwarfs were reobserved to improve the accuracy of their metallicity.

The rest 52 observed galaxies are selected to reside in the LV. They represent mostly a fainter part of the total subsample of the LV void galaxies. The currently updated list comprises of 243 LV void objects. Of 39 objects with the well detected strong lines, nine new void galaxies appeared to be very metal-poor, with $12+\log(\text{O}/\text{H}) \lesssim 7.39$ dex. Of them, two more XMP dwarfs are found, with $12+\log(\text{O}/\text{H}) = 7.07$ and 7.20 dex.

Summarising the results, presented here and the related discussion, we draw the following conclusions:

(i) The spectroscopy of 8 remaining ‘candidate’ XMP dwarfs from the sample of 60 objects residing in the nearby voids, results in the discovery of two additional XMP dwarfs, with $12+\log(\text{O}/\text{H}) \sim 7.19 - 7.20$ dex ($\sim Z_{\odot}/30$).

(ii) The almost completed program of search for void XMP dwarfs results in 11 new objects with $Z_{\text{gas}} = Z_{\odot}/50 - Z_{\odot}/30$, that comprises ~ 20 per cent of the selected

candidates. In addition, 23 very low-metallicity dwarfs ($Z_{\text{gas}} = Z_{\odot}/30 - Z_{\odot}/20$) are found, that is ~ 40 per cent of the initial list. This finding increases substantially the number of the known nearby very metal-poor dwarfs and allows us to conduct a deeper study of their individual and group properties and of their possible relation to Very Young Galaxies.

(iii) The first results are presented for the on-going project of the studying a subsample of 243 NVG galaxies residing in the Local Volume. Of 52 observed objects only 37 appeared in real to reside in the nearby voids, while the rest 15 had the wrong radial velocities in HyperLEDA.

(iv) The strong lines of Oxygen are detected and its abundance is estimated in 32 of these 37 NVG objects, with the total range of $12+\log(\text{O}/\text{H})$ of 7.07 dex to ~ 8.0 dex.

(v) The addition of the other available data on the LV void dwarfs allows us to probe the relation between $12+\log(\text{O}/\text{H})$ and M_{B} on a sample of ~ 90 objects. The general trend of the reduced metallicity for a given luminosity, already known from our earlier studies of the nearby void galaxies, is also well seen on the LV void galaxies. Besides, on this compilation of the LV void galaxies, we find a large scatter in O/H for a fixed M_{B} . Partly, the reason of this effect can be the presence in the LV void sample of galaxies in the 'bordering' regions of voids.

(vi) The studied void galaxies show a wide range of the star-forming activity. While the most typical dwarfs, dIrrs and late Spirals, show several SF regions, we find four new dTr galaxies with the substantial neutral gas reservoir and the absent or very subtle signs of the current/recent SF.

(vii) Two Local Volume HI objects, HIPASS J1614-72 and AGC208329 appear to have a mistaken optical identification. The search for their alternative optical counterparts did not reveal potential candidates. Since the full census of the LV population has the important implications for comparison of the LV with cosmological simulations, the understanding of the nature of these HI objects will take special efforts, including their HI-mapping and the improvement of their position accuracy.

ACKNOWLEDGEMENTS

This work is based on observations obtained with the Southern African Large Telescope (SALT), programs 2017-2-MLT-001, 2020-2-MLT-005, 2022-1-MLT-003 (PI: Kniazev). The reported study was funded by Russian Science Foundation according to the research project 22-22-00654. AYK acknowledges support from the National Research Foundation (NRF) of South Africa. We thank the anonymous reviewer for the useful comments and suggestions, which allowed us to improve the content and clarity of the paper. The use of the HyperLEDA database is greatly acknowledged. This research has made use of the NASA/IPAC Extragalactic Database (NED) which is operated by the Jet Propulsion Laboratory, California Institute of Technology, under contract with the National Aeronautics and Space Administration. We also acknowledge the great effort of the ALFALFA team which opened access to the nearby Universe gas-rich dwarfs with low or moderate SFR and thus helped us to identify the majority of very low metallicity galaxies of this study.

We also acknowledge the use of the SDSS and Legacy

surveys databases. Funding for the Sloan Digital Sky Survey (SDSS) has been provided by the Alfred P. Sloan Foundation, the Participating Institutions, the National Aeronautics and Space Administration, the National Science Foundation, the U.S. Department of Energy, the Japanese Monbukagakusho, and the Max Planck Society. The SDSS Web site is <http://www.sdss.org/>. The SDSS is managed by the Astrophysical Research Consortium (ARC) for the Participating Institutions.

The DESI Legacy Imaging Surveys consist of three individual and complementary projects: the Dark Energy Camera Legacy Survey (DECaLS), the Beijing-Arizona Sky Survey (BASS), and the Mayall z-band Legacy Survey (MzLS). DECaLS, BASS and MzLS together include data obtained, respectively, at the Blanco telescope, Cerro Tololo Inter-American Observatory, NSF's NOIRLab; the Bok telescope, Steward Observatory, University of Arizona; and the Mayall telescope, Kitt Peak National Observatory, NOIRLab. NOIRLab is operated by the Association of Universities for Research in Astronomy (AURA) under a cooperative agreement with the National Science Foundation. Pipeline processing and analyses of the data were supported by NOIRLab and the Lawrence Berkeley National Laboratory (LBNL). Legacy Surveys also uses data products from the Near-Earth Object Wide-field Infrared Survey Explorer (NEOWISE), a project of the Jet Propulsion Laboratory/California Institute of Technology, funded by the National Aeronautics and Space Administration. Legacy Surveys was supported by: the Director, Office of Science, Office of High Energy Physics of the U.S. Department of Energy; the National Energy Research Scientific Computing Center, a DOE Office of Science User Facility; the U.S. National Science Foundation, Division of Astronomical Sciences; the National Astronomical Observatories of China, the Chinese Academy of Sciences and the Chinese National Natural Science Foundation. LBNL is managed by the Regents of the University of California under contract to the U.S. Department of Energy.

DATA AVAILABILITY

The data underlying this article are available in Appendices A, B and C, which are available only in the on-line supplementary materials of the paper.

REFERENCES

- Alam S., Albareti F.D., Allende Prieto C., et al. 2015, *ApJS*, 219, 12
- Aller H.L., 1984, *Physics of Thermal Gaseous Nebulae* (Dordrecht, Reidel)
- Annibali F., La Torre V., Tosi M., et al., 2019, *MNRAS*, 482, 3892
- Aragon-Calvo M.A., & Szalay A.S., 2013, *MNRAS*, 428, 3409
- Asplund M., Grevesse N., Sauval A. J., Scott P., 2009, *ARA&A*, 47, 481
- Aver E., Berg D.A., Hirschauer A.S., Olive K.A., Pogge R.W., Rogers N.S.J., Salzer J.J., Skillman E.D., 2022, *MNRAS*, 510, 373

- Berg D.A., Skillman E.D., Marble A., et al. 2012, ApJ, 754, 98
- Brocklehurst M., 1971, MNRAS, 153, 471
- Buckley, D.A.H., Swart, G.P., Meiring, J.G., 2006, SPIE, 6267
- Burgh, E.B., Nordsieck, K.H., Kobulnicky, H.A., Williams, T.B., O'Donoghue, D., Smith, M.P., Percival, J.W., 2003, SPIE, 4841, 1463
- Cannon J., Giovanelli R., Haynes M., et al., 2011, ApJL, 739, 22
- Chengalur J.N., Pustilnik S.A., 2013, MNRAS, 428, 1579
- Chengalur J.N., Pustilnik S.A., Egorova E.S., 2017, MNRAS, 465, 2342
- Crawford S. M. et al., 2010, in Silva D. R., Peck A. B., Soifer B. T., Proc. SPIE Conf. Ser. Vol. 7737, Observatory Operations: Strategies, Processes, and Systems III. SPIE, Bellingham, p. 773725
- Dey A., Schlegel D., Lang D., et al. 2019, AJ, 57, id. 168
- Filippenko A.V., 1982, PASP, 94, 715
- Fioc M., Rocca-Volmerange B., 1999, astro-ph/9912179
- Gottlöber S., Lokas E.L., Klypin A., Hoffman Y., 2003, MNRAS, 344, 715
- Guseva N.G., Papaderos P., Meyer H.T., Izotov Y.I., Fricke K.J., 2009, A&A, 505, 63
- Hauberg N.C., Salzer J.J., Cannon J.M., Marshall M.V., 2015, ApJ, 800, 121
- Haynes M.P., Giovanelli R., Kent B.R., et al. 2018, ApJ, 861, 49
- Hirschauer A.S., Salzer J.J., Skillman E.D., et al. 2016, ApJ, 822, 108
- Hsyu T., Cooke R.J., Prochaska J.X., Bolte M., 2017, ApJ Lett., 845, L22
- Huchtmeier W., Karachentsev I.D., Karachentseva V.E., Ehle M., 2000, A&A Suppl. 141, 469
- Huchtmeier W.K., Karachentsev I.D., Karachentseva V.E., 2003, A&A, 401, 483
- Izotov Y.I., Thuan T.X., 2007, ApJ, 665, 1115
- Izotov Y.I., Thuan T.X., Lipovetsky V.A., 1994, ApJ, 435, 647
- Izotov Y.I., Thuan T.X., Lipovetsky V.A., 1997, ApJS, 108, 1
- Izotov Y.I., Stasińska G., Meynet G., Guseva N.G., Thuan T.X., 2006, A&A, 448, 955
- Izotov Y.I., Thuan T.X., Guseva N.G., 2012, A&A, 546, A122
- Izotov Y.I., Guseva N.G., Fricke K.J., Henkel C., 2019, A&A, 523, A40
- Izotov Y.I., Thuan T.X., Guseva N.G., 2021, MNRAS, 504, 3996
- Karachentsev I.D., Makarov D.I., Kaisina E.I., 2013, AJ, 145, 101
- Karachentsev I.D., Makarova L.N., Tully R.B., Wu P.-F., Kniazev A.Y., 2014, MNRAS, 443, 1281
- Karachentsev I.D., Makarova L.N., Koribalski B.S., Anand G.S., Tully R.B., Kniazev A.Y., 2023, MNRAS, 518, 5893
- Kesseli A.Y., West A.A., Veyette M., Harrison B., Feldman D., Bochanski J.J., 2017, ApJS, 230, a.i. 16, 21 pp.
- Kilborn V.A., Webster R.L., Staveley-Smith L., et al. 2002, AJ, 124, 690
- Kniazev A.Y., 2022, Astrophysical Bulletin, 77, 334-346
- Kniazev A.Y., Pustilnik S.A., Grebel E.K., Lee H., Pramskij A.G., 2004, ApJS, 153, 429
- Kniazev A.Y., Grebel E.K., Pustilnik S.A., Pramskij A.G., Zucker D., 2005, AJ, 130, 1558
- Kniazev A.Y., Egorova E.S., Pustilnik S.A., 2018, MNRAS, 479, 3842
- Kobulnicky, H.A., Nordsieck, K.H., Burgh, E.B., Smith, M.P., Percival, J.W., Williams, T.B., O'Donoghue, D., 2003, SPIE, 4841, 1634
- Koleva M., Prugniel P., Bouchard A., Wu Y., 2009, A&A, 501, 1269
- Kreckel K., Platen E., Aragon-Calvo M.A., van Gorkom J.H., van de Weygaert R., van der Hulst J.M., Beygu B., 2012, AJ, 144, 16
- Makarov D.I., Uklein R.I., 2012, Astrophys.Bull., 67, 135
- Makarov D.I., Prugniel P., Terekhova N., Courtois H., Vauglin I., 2014, A&A, 570, A13
- Mamon G.A., Trevisan M., Thuan T.X., Galazzi A., 2020, MNRAS, 492, 1791
- McQuinn K., Cannon J.M., Dolphin A.E., et al., 2014, ApJ, 785, 3
- O'Donoghue D., et al. 2006, MNRAS, 372, 151
- Papaderos P., Östlin G., 2012, A&A, 537, A126
- Patiri S.G., Prada F., Holtzman J., Klypin A., Betancort-Rijo J., 2006, MNRAS, 372, 1710
- Perepelitsyna Y.A., Pustilnik S.A., Kniazev A.Y. 2014, Astrophys.Bull., 69, 247 (arXiv:1408.0613)
- Pilyugin L.S., Thuan T.X., 2005, ApJ, 631, 231
- Pustilnik S.A., Tepliakova A.L., 2011, MNRAS, 415, 1188
- Pustilnik S.A., Martin J.-M., 2016, A&A, 596, A86
- Pustilnik S.A., Zasov A.V., Kniazev A.Y., Pramsky A.G., Ugryumov A.V., Burenkov A.N., 2003, A&A, 400, 841-858
- Pustilnik S.A., Kniazev A.Y., Pramskij A.G., 2005, A&A, 443, 91
- Pustilnik S.A., Tepliakova A.L., Kniazev A.Y., Martin J.-M., Burenkov A.N., 2010, MNRAS, 401, 333
- Pustilnik S.A., Martin J.-M., Tepliakova A.L., Kniazev A.Y., 2011, MNRAS, 417, 1335
- Pustilnik S.A., Martin J.-M., Lyamina Y.A., Kniazev A.Y., 2013, MNRAS, 432, 2224
- Pustilnik S.A., Perepelitsyna Y.A., Kniazev A.Y., 2016, MNRAS, 463, 670
- Pustilnik S.A., Tepliakova A.L., Makarov D.I., 2019, MNRAS, 482, 4329 (PTM19)
- Pustilnik S.A., Egorova E., Perepelitsyna Y.A., Kniazev A.Y., 2020a, MNRAS, 492, 1078
- Pustilnik S.A., Kniazev A.Y., Perepelitsyna Y.A., Egorova E.S., 2020b, MNRAS, 493, 830 (PKPE20)
- Pustilnik S.A., Egorova E.S., Kniazev A.Y., Perepelitsyna Y.A., Tepliakova A.L., Burenkov A.N., Oparin D.V., 2021, MNRAS, 507, 494
- Pustilnik S.A., Tepliakova A.L., Perepelitsyna Y.A., Kniazev A.Y., Makarova L.N., Burenkov A.N., Kotov S.S., Malygin E.A., 2022a, MNRAS, 516, 6180
- Pustilnik S., Perepelitsyna Y., Tepliakova A., Kniazev A., Egorova E., Chengalur J., Kurapati S., 2022b, in Proc. of conf. "The Multifaceted Universe: Theory and Observations - 2022" (MUTO2022), PoS, id.26 (arXiv:2212.0564)
- Rojas R.R., Vogeley M.S., Hoyle F., Brinkmann J., 2005, ApJ, 624, 571
- Schlafly E.F., Finkbeiner D.P., 2011, ApJ, 737, 103, 13pp.
- Searle L., Sargent W.L.W., 1972, ApJ, 173, 25
- Skillman E., Salzer J.J., Berg D.A., et al., 2013, AJ, 146, 3
- Stasińska G., 1990, A&AS, 83, 501

- Stasińska G., Izotov Y.I., 2003, *A&A*, 397, 71
Tully B., Shaya E.J., Karachentsev I.D., Courtois H.M.,
Kocevski D.D., Rizzi L., Peel A., 2008, *ApJ*, 676, 184
Tweed D.P., Mamon G.A., Thuan T.X., Cattaneo A., Dekel
A., Menci N., Calura F., Silk J., 2018, *MNRAS*, 477, 1427
van de Weygart R., 2016, in *The Zel'dovich Universe: Gen-
esis and Growth of the Cosmic Web*, Proc. IAU Sympo-
sium, V.308, pp. 493-523,
van Zee L., 1997, *AJ*, 119, 2757
van Zee L., Haynes M.P., 2006, *ApJ*, 636, 214
van Zee L., Haynes M.P., Skillman E., 2006, 637, 269
Whitford A.E., 1968, *AJ*, 63, 201